THE EFFECTS OF CHEMICAL SHORT-RANGE ORDER ON
CRYSTALLIZATION PATHWAY IN TERNARY MARGINAL GLASS
FORMING ALLOYS

A THESIS SUBMITTED TO
THE GRADUATE SCHOOL OF NATURAL AND APPLIED SCIENCES
OF
MIDDLE EAST TECHNICAL UNIVERSITY

BY

EMEL ERDAL

IN PARTIAL FULFILLMENT OF THE REQUIREMENTS
FOR
THE DEGREE OF MASTER OF SCIENCE
IN
METALLURGICAL AND MATERIALS ENGINEERING

SEPTEMBER 2021

Approval of the thesis:

THE EFFECTS OF CHEMICAL SHORT-RANGE ORDER ON CRYSTALLIZATION PATHWAY IN TERNARY MARGINAL GLASS FORMING ALLOYS

submitted by **EMEL ERDAL** in partial fulfillment of the requirements for the degree of **Master of Science** in **Metallurgical and Materials Engineering, Middle East Technical University** by,

Prof. Dr. Halil Kalıpçılar
Dean, Graduate School of **Natural and Applied Sciences**   _____

Prof. Dr. C. Hakan Gür
Head of the Department, **Metallurgical and Materials Eng.**   _____

Prof. Dr. Y. Eren Kalay
Supervisor, **Metallurgical and Materials Eng., METU**   _____

Examining Committee Members:

Prof. Dr. Arcan F. Dericioğlu
Metallurgical and Materials Engineering, METU   _____

Prof. Dr. Y. Eren Kalay
Metallurgical and Materials Engineering, METU   _____

Assoc. Prof. Dr. Sezer Özerinç
Mechanical Engineering, METU   _____

Assoc. Prof. Dr. Benat Koçkar
Mechanical Engineering, Hacettepe University   _____

Assist. Prof. Dr. Eda Aydoğan
Metallurgical and Materials Engineering, METU   _____

Date: 08.09.2021

I hereby declare that all information in this document has been obtained and presented in accordance with academic rules and ethical conduct. I also declare that, as required by these rules and conduct, I have fully cited and referenced all material and results that are not original to this work.

Name Last name: Emel Erdal
Signature:

ABSTRACT

THE EFFECTS OF CHEMICAL SHORT-RANGE ORDER ON CRYSTALLIZATION PATHWAY IN TERNARY MARGINAL GLASS FORMING ALLOYS

Erdal, Emel
Master of Science, Metallurgical and Materials Engineering
Supervisor: Prof. Dr. Y. Eren Kalay

September 2021, 77 pages

Among all the metallic glass-forming systems, Al-based marginal glass-forming alloys (Al-RE or Al-TM-RE) have been recently received significant attention due to their unusual devitrification behavior. The population of nanocrystals developed in the amorphous matrix can reach up to 10^{24} m^{-3} upon crystallization, which cannot be explained by classical nucleation theory. Our previous studies on binary $Al_{90}RE_{10}$ (RE: Sm, Tb, Y) systems have shown that the topological medium-range order, which is inherited from the liquid state, is effective in the formation of nanocrystals upon devitrification. In this study, we have examined the effects of chemical order on devitrified ternary metallic glass systems. Particularly, $Al_{90}Sm_5Tb_5$ and $Al_{90}Y_5Tb_5$ ternary metallic glasses were investigated by differential scanning calorimetry (DSC), transmission electron microscopy (TEM), atom probe tomography (APT), and high energy synchrotron X-Ray diffraction (HEXRD) methods. It was observed that although the total amount of RE is constant, the substitution of Tb with 5% of Y or Sm has changed the devitrification path compared to $Al_{90}RE_{10}$ (RE: Sm, Tb, Y) binary systems. The traditional fcc-Al nanocrystallization event observed in binary Al-RE metallic glass systems was found to be altered in $Al_{90}Sm_5Tb_5$ glassy alloys. Instead, the formation of intermetallic

phases with fcc-Al nanocrystals embedded inside is observed in TEM analysis. This behavior is also supported by DSC results, where a sharp exothermic transformation peak with a significant enthalpy change replaced the traditional low intensity and broad fcc-Al nanocrystallization peak. This work has been supported by AFOSR under contract number FA9550-20-1-0261.

ÖZ

MARJİNAL CAM OLUŞTURAN ÜÇLÜ ALAŞIMLARDA KİMYASAL KISA ERİM DÜZENİNİN YAPISAL DÖNÜŞÜM MEKANİZMASINA ETKİLERİ

Erdal, Emel
Yüksek Lisans, Metalurji ve Malzeme Mühendisliği
Tez Yöneticisi: Prof. Dr. Y. Eren Kalay

Eylül 2021, 77 sayfa

Bütün metalik cam oluşturan sistemler arasında, Al bazlı camsı alaşımlar (Al-RE ya da Al-TM-RE), alışılmadık devitrifikasyon davranışları sebebiyle son dönemlerde büyük ilgi görmektedir. Kristallenme esnasında amorf matris içerisinde gelişen nanokristal populasyonu 10^{24} m^{-3} değerine kadar ulaşabilmekte ve bu durum klasik çekirdeklenme teorisiyle açıklanamamaktadır. Al$_{90}$RE$_{10}$ (RE: Sm, Tb, Y) ikili alaşım sistemleri üzerinde daha önce yapılan çalışmalar, sıvı yapıdan süregelen topolojik orta erimli düzenin, yüksek yoğunluklu nanokristal oluşumunda etkili olduğunu göstermiştir. Bu çalışma kapsamında ise, kimyasal düzenin devitrifike üçlü metalik cam sistemleri üzerindeki etkileri araştırılmıştır. Diferansiyel taramalı kalorimetre (DSC), geçirimli elektron mikroskobu (TEM), üç boyutlu atom prob tomografisi (APT) ve yüksek enerjili sinkrotron X-ışını kırınımı (HEXRD) karakterizasyon methodları kullanılarak özellikle Al$_{90}$Sm$_5$Tb$_5$ ve Al$_{90}$Y$_5$Tb$_5$ üçlü metalik cam alaşımları incelenmiştir. Toplam nadir toprak elementi (RE) miktarı sabit olmasına rağmen, Tb atomlarının %5 Y ya da Sm ile yer değiştirmesinin, Al$_{90}$RE$_{10}$ (RE: Sm, Tb, Y) ikili sistemlere kıyasla, devitrifikasyon yolunu değiştirdiği gözlemlenmiştir. Al-RE ikili alaşım sistemlerinde görülmeye alışkın olunan geleneksel fcc-Al

nanokristallenme eğilimi, $Al_{90}Sm_5Tb_5$ alaşımında farklılık göstermiştir. Bunun yerine, TEM analizlerinde intermetalik fazlar içerisine gömülmüş ymk-Al nanokristallerin oluşumu gözlemlenmiştir. Bu davranış, geleneksel düşük şiddetli ve geniş ymk-Al nanokristallenme sinyalinin yerini sivri, belirgin entalpi değişimli ısı veren dönüşüm sinyalinin aldığı DSC sonuçlarıyla da desteklenmiştir. Bu araştırma FA9550-20-1-0261 kontrak numarası ile AFOSR tarafından desteklenmiştir.

Anahtar Kelimeler: Marjinal metalik cam, Devitrifikasyon, Üç boyutlu atom prob tomografisi, Geçirimli elektron mikroskobu, Sinkrotron X-ışını kırınımı

TABLE OF CONTENTS

LIST OF TABLES

LIST OF FIGURES

LIST OF ABBREVIATIONS

ABBREVIATIONS

APT	Atome Probe Tomography
BF	Bright-Field TEM Image
BMG	Bulk Metallic Glass
DF	Dark Field
DSC	Differential Scanning Calorimetry
EDS	Electron Dispersive Spectroscopy
FCC	Face Centered Cubic
FIB	Focused Ion Beam
GFA	Glass Forming Ability
HEXRD	High Energy X-Ray Diffraction
HRTEM	High Resolution Transmission Electron Microscopy
JMA	Johnson-Mehl-Avrami
MGF	Marginal Glass Former
MRO	Medium-Range-Order
RE	Rare-Earth Element
SAED	Selected Area Electron Diffraction
SEM	Scanning Electron Microscopy
SMA	Simple Moving Average
SRO	Short-Range-Order
TEM	Tranmission Electron Microscopy
WDS	Wavelength Dispersive Spectroscopy
XRD	X-Ray Diffraction

CHAPTER 1

INTRODUCTION

1.1   History of Metallic Glasses

Humankind has been using many materials such as wood, metal, glass, and their combinations as an instrument to fulfill their daily and long-term needs. With the beginning of the 20th century, new material came into view with tremendous potential and attracted scientists' significant interest and research efforts. This non-crystalline material that has a wide area of usage is called metallic glass. Metallic glasses have brought great excitement into the science world due to their high hardness, which gives good abrasion and wears resistance, high specific strength, promising thermal, magnetic, and environmental properties [1].

In 1960, Duwez and his team, who had the purpose of getting amorphous solid alloy by splat quenching of the melt, rapidly quenched the Au-Si alloy from 1300 °C to room temperature obtained the first example of metallic glass [2], [3]. In 1961, Cohen and Turnbull showed that highly disordered alloys with a low melting eutectic point are more suitable for glass formation. This result shows a way to search for alloys favorable to be quenched into a glass [4]. Chen and Turnbull, in 1969, published the results of Pd-Au-Si, Pd-Ag-Si, and Pd-Cu-Si ternary metallic glass systems at different considerably lower cooling rates [5]. Earliest bulk glass former, Pd- Cu- Si ternary system, was obtained by Chen and Turnbull [6], followed by studies of Au-Pb-Sn alloy by Lee, Kendall, and Johnson [7].

Meanwhile, Turnbull, Greer, and Drehman obtained Pd- Ni-P ternary bulk metallic glass at a less than 100 K/s^{-1} cooling rate and 1 cm thickness [8]. Later, Inoue and

colleagues presented the outputs on a novel system bulk metallic glass study, including La- Al-Ni-Cu and other promising alloys [9], [10]. In the following years, Inoue and his research group studied different compositions and techniques, which led them to acquire up to 5 cm diameter of bulk metallic glass outcome. Many different metallic glass production techniques have been developed, and the related interest in the subject of metallic glass has increased since then.

1.2   Marginal Glass Formers

Metallic glasses are often classified into two subcategories regarding cooling rate as bulk metallic glasses (BMG) and marginal glass formers (MGF). As the name indicates, it is possible to produce bulk metallic glasses with certain thicknesses since BMGs require cooling rates lower than 10^3 K/s. In 1982 Turnbull et al. successfully produced $Pd_{40}Ni_{40}P_{20}$ metallic glass having almost 10 mm thickness by a cooling rate of 10 K/s [11]. In contrast, marginal glass formers can only be acquired by rapid cooling techniques (i.e., melt-spinning) in which the solidification rate reaches 10^5-10^6 K/s to suppress crystallization [12]. Therefore, the shapes of MGFs are restricted to thin films, ribbons, or small particles [13]. MGFs fall into two categories which are Al-based and Fe-based marginal glass formers [14].

1.3   Aluminum Based Marginal Glass formers

Since the first outcome of metallic glass in 1960, although various metallic alloys have been used in order to get qualified products, the first successful Al-based metallic glass, which has a broad composition range for X-Al-B (X=Fe, Ni and Co) were obtained by Inoue and his group in 1981. As aluminum has a metallic character in the amorphous state of these alloys, it may disperse substitutionally, so contacting of aluminum-aluminum atoms are occurred quickly in the amorphous phase due to its larger atomic size. Therefore, it is observed that a wide formation range of

amorphous parts occurred in affluent aluminum areas [15]. These studies were promising and attracted much attention among materials scientists. However, due to the brittleness of these systems and relatively low tensile strength, about 50-150 MPa, using these systems as engineering materials in real life was not possible [16]. Two research groups in 1988 came up with new Al-based systems, including transition metals (TM) and rare-earth elements (RE), with enhanced tensile strength and elasticity, produced by the melt spinning method. Ribbons were bent in half, and no fracture was observed [17], [18]. An average cooling rate of 10^5-10^6 K/s was found to be necessary to quench a high-temperature molten alloy into the solid amorphous phase and suppress diffusion.

Al-based MGF alloys possess superior properties like lightweight, high specific strength, and good corrosion resistance, which open up possibilities for finding new high strength low-density alloy, even though this system's glass-forming ability (GFA) is comparatively low [12]. The GFA, or in other words, the ease of devitrification, is a critical property for all glass-forming systems in order to understand how metallic glasses can be obtained or how the properties of these systems can be enhanced. Avoiding local ordered structure, which leads to crystallization, is associated with the glass-forming ability [19]. Controlling the cooling rate is crucial to control the formation of glassy structures and the size of the amorphous alloy. In Figure 1.1 schematic representation of a time-temperature-transformation (TTT) diagram is shown. The crystallization occurs between the temperatures T_l and T_g, and the crystallization can be avoided by having cooling rates equal to or higher than R_c [20].
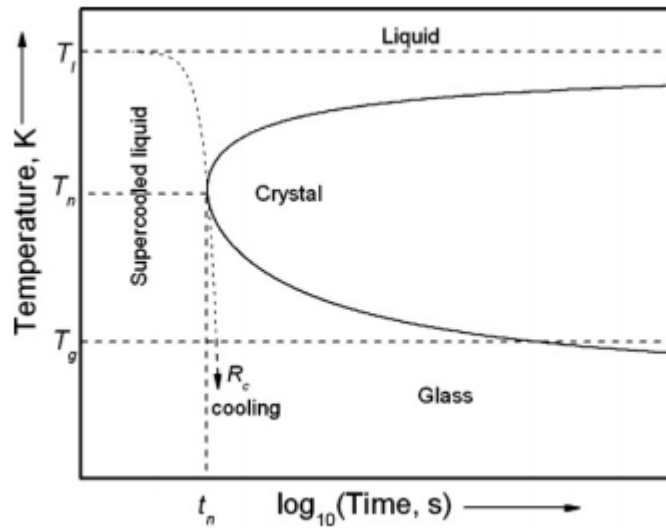
Figure 1.1 Schematic TTT diagram showing the crystallization behavior of a glass-forming liquid (Adopted from [20])

In 2000, Inoue [21] revealed three empirical conditions to stable the supercooled melts and to have high GFA, which gives better mechanical and thermal properties of MGs as follows:

1. Having more than three elements for creating a multi-component system
2. Having atomic size difference above %12
3. Having negative enthalpy of mixing among components of the system

The constituent elements more than three kinds with large atomic size ratios
above 12 % and negative heats of mixing

Increase in the degree of dense random packed structure
(topological and chemical points of view)

Formation of liquid with new atomic configurations
and multicomponent interactions on a short-range scale

Increase of solid/liquid
interfacial energy

Difficulty of
atomic rearrangement
$\left(\begin{array}{c}\text{decrease of atomic diffusivity,}\\ \text{increase of viscosity}\end{array}\right)$

Necessity of
atomic rearrangement
on a long-range scale
for crystallization

Suppression of
nucleation
of a crystalline phase

Increase of T_g

Suppression of growth
of a crystalline phase

Decrease of T_m, Increase of T_g/T_m

Figure 1.2 Flow chart for having high GFA and stable melt, fulfilling Inoue's three
rules. (Adopted from [21])

New criteria have been suggested to discuss GFA recently [22]. These approaches
can be divided into four groups:

1. Using fundamentals of transition temperatures, T_g, T_x, T_l, and their
   combinations
2. Using thermodynamic data to predict and explain GFA in a given system
3. Using the physical characteristic of a given alloy like crystallization
   behavior, viscosity
4. Using computational methods to predict GFA by simulating

1.4 Production Methods

As mentioned before, metallic glasses are divided into two subclasses: BMG, which
requires cooling rates lower than 10^3 K/s, and marginal glass formers, which require
higher cooling rates (10^5-10^6 K/s). Therefore, in addition to methods used for MGF
production, BMGs can be manufactured by cheaper and less complicated production

methods such as conventional casting. In this section, the production methods of MGFs are briefly summarized and categorized into three: rapid solidification (RSP), vapor state (VSP), and solid-state processes.

1.4.1   Rapid Solidification Processes (RSP)

As the name implies, the rapid solidification processes consist of solidifying the molten alloy rapidly to prevent crystallization. These simple and effective methods have been used since the first metallic glass Au-Si system was obtained using a rapid solidification technique called splat quenching. In this method, the rate of absorbing heat from the system is critical to controlling the glassy structure. Other common RSP methods are droplet, jet, surface melting, melt spinning, and casting [23], [24].
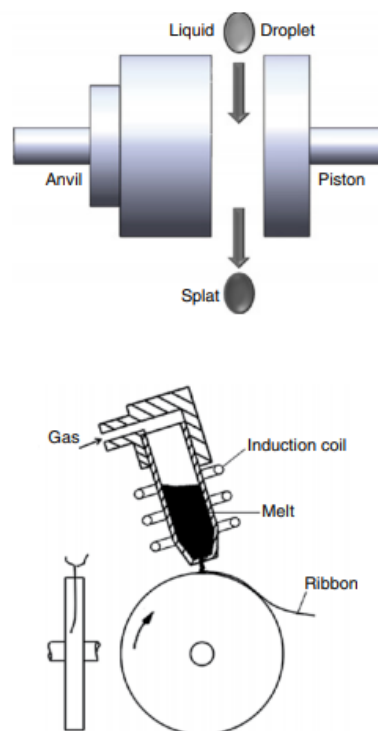
Figure 1.3 Representation of splat quenching technique (above) and melt spinning method (below) (Adopted from [23])

In this work, the melt spinning method is used to produce the amorphous ribbon samples. The principle of melt spinning is simple and the same as other RSP methods: cooling the melt at a very high rate. The liquid alloy is pushed through the nozzle and created a puddle on the roller. Surface tension and the stream's counteracting forces decide the form of the puddle. Only a few microns are affected by shear, so liquid stays on the surface due to low liquid viscosity. Heat exchange between the surface of roller and liquid is so large that melt on the surface turns into a ribbon and releases the surface due to centrifugal force [25]. In order to prevent the oxidation of molten metal, the process is carried out under a high purity noble gas atmosphere like argon or helium. Melt spinning is commonly chosen for manufacturing Al-based metallic glasses [26]. In figure 1.3, the schematic representation of splat quenching and melt spinning are displayed.

1.4.2 Vapor State Processes (VSP)

The purpose of vapor state processes (VSP) is to vaporize the material and condense it onto the surface to be deposited. Physical vapor deposition (PVD), chemical vapor deposition (CVD), Ion Implantation, and magnetron sputtering are typical examples of VSP [27], [28]. Generally, the cooling rate reaches 10^{12} K/s, and the coating substrate is kept at very low temperatures. Therefore, developing a non-crystalline phase is comparatively easy. This method is commonly used in scientific experiments as well as electronic and magnetic industries. Products created by VSP are sensitive to impurities which are considered as a cause for forming amorphous structures. [22]

1.4.3 Solid-State Processes

Other techniques like mechanical alloying, milling and cold rolling are called solid-state processes or solid-state amorphization reactions [29]. After executing severe plastic deformation onto a system, free energy and temperature increase are observed

since the defected atomic arrangement is created by vacancies, dislocations, stacking errors, and grain boundaries [27]. This creates negative heat of mixing enthalpy (ΔH_{mix}) and suppresses the nucleation of stable intermetallic alloy. With decreased grain size, distorted lattice with strain, and disintegration of smaller atoms like Al in the lattice, the structure transforms from crystalline to amorphous to decrease its energy. In order to obtain better mechanical properties, parameters like temperature, cycle number, energy (in high and low energy mills), and time should be carefully controlled [30].

1.5   Chemical and Structural Characterization Methods

1.5.1   High Energy X-Ray Diffraction (HEXRD)

High energy X-Ray diffraction is a powerful tool for structural characterization, and this type of radiation can be obtained by a synchrotron light source. A synchrotron is a well-designed accelerator based on a fundamental principle; if an electron in movement is forced to change its direction, energy can be emitted. An X-ray can be obtained if this movement is fast enough. X-ray produced by synchrotron has superior qualities that make them worthy of utilizing. Energized beams can be created over a broad extent of energies because of continuous energy dispersion. Wide E/ λ range, where E is the energy and λ is the wavelength, helps for a better investigation since high E allows deep penetration into the sample while low λ permits studying parts on a small scale [31].
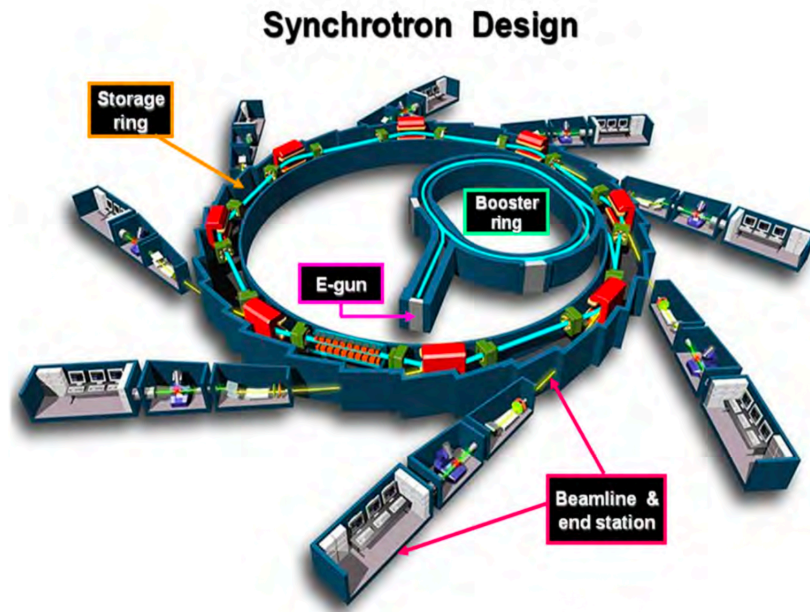
Figure 1.4 Schematic representation of the Soleil synchrotron facility (Adopted from [32])

Figure 1.4 represents a schematic drawing of the Soleil synchrotron light source. A Synchrotron consists of four main components: the electron gun, the booster ring, storage ring, and beamline. The electron gun, also known as the linac, is a high voltage vacuumed cathode that is warmed up for energizing electrons, makes them emit from the surface and supplies enough electrons to the system. A Booster is an accelerator where electrons are injected by an electron gun and energized through an RF voltage source before driving into the storage ring. The storage ring is a circular closed tube where electrons travel inside. This structure also contains bending magnets that deflect electrons from their orbit and emit light, containing a broad range of spectrum from microwave to X-Ray. The beamline is a section that X-rays are emitted by electrons, directed, and collected. In beamline, light is forced to travel from storage ring to beamline, and at optic part, light is focused with a specific wavelength. These highly energized X-rays are collected and controlled in every aspect [31], [33].

1.5.2   Transmission Electron Microscopy (TEM)

Transmission electron microscopy (TEM) is an advanced method used to investigate solid materials' morphology, atomic structure, faults, and transformation phases. The high-resolution transmission electron microscopy (HRTEM) allows imaging at the atomic scale. In addition to 2D imaging, this method is also used to obtain diffraction patterns. Unlike X-Ray spectroscopy, the selected area electron diffraction (SAED) pattern can be collected from minimal areas with better resolutions [12].
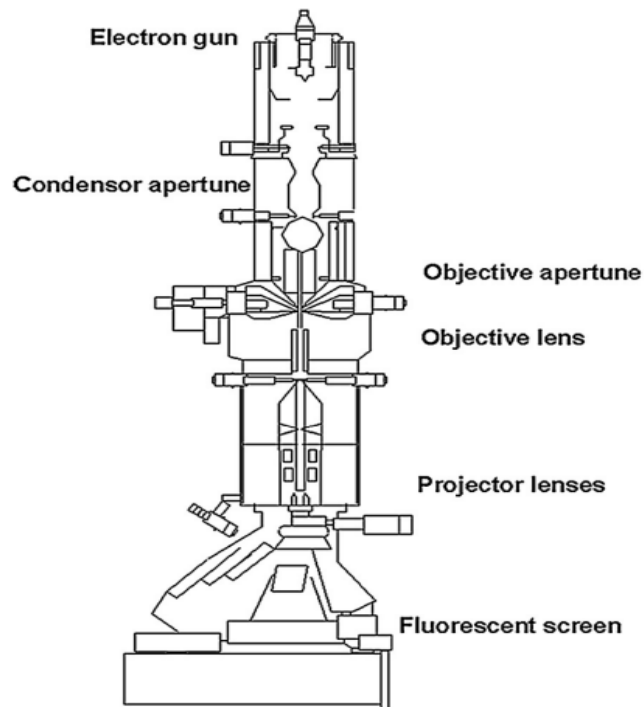
Figure 1.5 Schematic representation of TEM (Adopted from [34])

A schematic representation of a TEM is presented in Figure 1.5. At the top of the microscope, an electron gun that generates electron beams is located. Beams are focused on electromagnetic lenses. Electrons act as negatively charged particles due to the wave-like nature of electrons, and electric and magnetic fields deflect these

beams and make them focused. These energized electrons are directed to sample under a vacuum to maintain the free path of electrons. These electrons can be diffracted or passed through material regarding energy level of electrons, density, and composition of the sample [35], [36]. Transmitted electrons are gathered by lenses to fluorescent screens, and a detailed 2-D visual image is created [34]. Sample should be prepared thin enough for electrons to penetrate. TEM can also be combined with EDS (Electron Dispersive Spectroscopy) to analyze chemical, elemental specimen analysis without any destructive test.

1.5.3   3D Atom Probe Tomography

Atom Probe Tomography (APT) is an advanced characterization tool used to analyze the chemical composition and create images in 3D. The APT is not a simulation and modeling method. The created 3D image is the real tomography of the sample. The elemental concentration is calculated by enumerating the atoms that reached the detector. With the analyses of APT data, atomic-scale properties and interatomic dispersion can be measured, such as a profile of concentration, formation of the clusters, crystal structure, and stages of precipitation. Although other systems can show structure at the sub-nanometer level, APT exhibits a wide range of compositional classification with very high resolution (0.1-0.3nm in depth and 0.3-0.5 nm laterally) [37], [38].

An APT specimen should be in the form of a sharp tip with a curvature of radius less than 50 μm. The sample is usually prepared by FIB with extensive Ga^+ ion milling. The working principle relies on ion evaporation from the specimen's tip by field-effect under high vacuum conditions. The sample is cooled down to cryogenic temperatures, and a high DC voltage is applied. When the sample is laser pulsed or voltage pulsed, individual ions evaporate and reach the 2D position-sensitive detector (PSD). The system is combined with a time to digital converter, which measures T_{event}. T_{event}, or in other words, time of flight, is the time passed between

the pulse and the arrival of the atom to the detector. The 2D detector defines the positions of atoms in the X and Y directions. By adding the time of flight data to the position information, the 3D mapping image is created [37], [39]. Figure 1.6 shows the schematic representation of the APT analyses where the atoms are field evaporated and collected through PSD. It is impossible to detect all the evaporated ions by PSD, but the ion efficiency can reach up to 80% with newly developed systems [38].
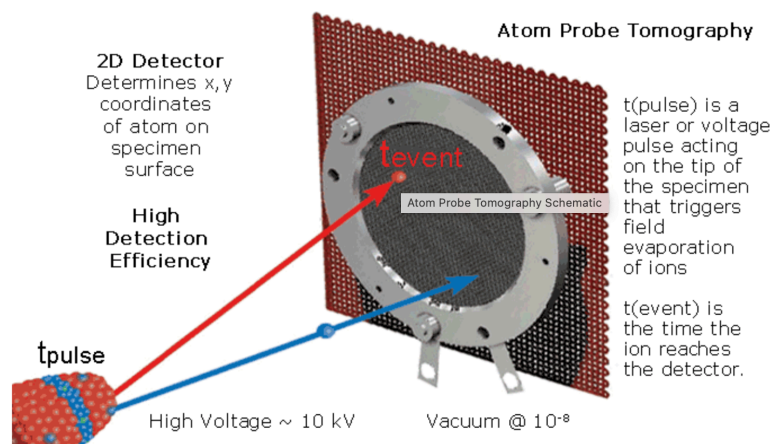
Figure 1.6 Schematic representation of the field evaporation during APT analysis (Adopted from [38])

For an APT experiment, it is crucial to optimize the parameters, which are the pulse rate, base temperature, detection rate, pulse fraction, and pulse energy, according to the material to be analyzed. Pulse rate is defined as the maximum rate which allows the mass to charge state ratio (m/n) scope of atoms taken by a single pulse for all voltages. The base temperature should be kept low in order to obtain a better resolution but should be determined according to other parameters. In voltage pulse mode, base temperature diversity results in yield differences. The mobility of residual gasses in the vacuum pan can be reduced by achieving lower sample temperatures [37], [39].

The APT analysis can be conducted in two different modes as the voltage pulse and the laser pulse modes. A solid-state HV generator is used to create a concise duration of negative voltage values for the voltage pulse mode. The generator works at a constant pulse rate. As the tip radius varies during the experiment, the pulse voltage alters to keep the ion detection rate constant. The balance between the pulse rate, detection rate, and pulse fraction is essential [37], [39]. The pulse rate determines the data quality, but it should be noted that as the voltage pulse is applied repeatedly, the applied stresses may result in cyclic fatigue and failure of the sample to be analyzed [40]. It is hard to analyze some samples, such as materials having poor electrical conductance, in voltage pulse mode. As the applied voltage moves through the specimen, it is attenuated, and therefore the efficiency of field evaporation decreases. Such samples can be analyzed in laser pulse mode.

In laser pulse mode, the controlled parameter is the laser pulse energy (LPE) which is defined as the total photon energy transferred by each pulse. The field evaporation process is temperature-dependent, and the thermal pulse resulted from the pulsing laser decreases the required electrostatic field. Hence, the stress on the specimen lowers, and the analysis quality increases. The inadequate LPE can result in unfavorable results similar to inadequate pulse fraction in voltage pulse mode. The overall evaluation shows that the LPE should be set to higher values for better results. However, an unnecessary increase in LPE might reveal concerns about surface migration, complex ion generation, and nonuniform spatial evaporation. Hence, the reconstruction of the actual positions of the ions becomes harder. In Table 1.1, the summary of experimental parameters and how they affect the analyses are presented. In the table, the sign "+" means the trend is improving, and the sign "-" means the effect is negative as the parameter changes.

Table 1.1 A summary of APT parameters and their effects on the data acquisition (Adopted from [37])

Acquisition parameter	Variable	General trend	Metrics	Comments	Primary tradeoff
Pulse rate ↑	f (Hz)	+ +	Background	Higher is better	Almost none except for practical considerations for TOF of all potential ion species
		−	m/n range	Exceptions: high-mass ions with long TOF or extremely poor thermal diffusivity materials in laser mode	
		−	Wrap around		
		−	Base temperature offset effects (laser)		
Base temperature ↑	T (K)	+ +	Analysis yield	Lower leads to better spatial resolution, Higher leads to better yield	Data quality vs. analysis yield
		− −	MRP		
		− −	Background		
		−	Heat flow (laser)		
		−	Surface diffusion		
Detection rate ↑	DR (ions/pulse)	+ +	Background	Higher is better	Data quality vs. analysis yield
		−	Analysis yield	Exception: poor yielding materials and materials prone to multi-hit behavior	
		−	MRP		
		−	Multi-hit performance		
Pulse fraction ↑ (voltage mode)	PF (%)	+ +	Compositional accuracy	Higher is better	Data quality vs. analysis yield
		+	Background	Exception: Extreme PF may limit MRP and pulse amplitude is hardware limited	
		−	Potential for PF decay		
		−	High cycle fatigue		
Laser pulse energy ↑ (laser mode)	LPE (nJ or pJ)	+ + +	Analysis yield	Higher leads to better yield	Data quality vs. analysis yield
		+ +	Background	Lower leads to better spatial resolution	
		+	MRP		
		+	Effective pulse fraction		
		−	Complex ion generation		
		− −	Surface migration		

CHAPTER 2

DEVITRIFICATION BEHAVIOR OF Al$_{90}$Sm$_5$Tb$_5$ AND Al$_{90}$Y$_5$Tb$_5$ TERNARY GLASSY ALLOYS

2.1   Introduction

Marginal glass-forming alloys are special among all metallic glasses with their unique crystallization behavior upon devitrification. In many Al-based (Al-RE-TM) alloy systems, it has been shown that these alloys devitrify into an anomalous nuclei density which cannot be explained by classical nucleation theory. In some of these alloy systems, the fcc-Al nanocrystal density can reach up to 10^{21}-10^{24} m^{-3}. Although many scientists have studied the thermodynamics and kinetics behind this behavior with experimental studies supported by modeling and simulation, the nucleation phenomenon still preserves some mysteries. Previous studies concluded that the rare-earth elements are responsible for this abnormal phase transformation. However, whether this effect is due to the chemical interactions or the topological effect of the rare-earth atoms is still unknown. In this chapter, we have investigated Al$_{90}$Sm$_5$Tb$_5$ and Al$_{90}$Y$_5$Tb$_5$. The rare-earth content in both alloys is 10%, but chemical interactions would be different. The first crystallization events of these Al$_{90}$Sm$_5$Tb$_5$ and Al$_{90}$Y$_5$Tb$_5$ metallic glasses are investigated by DSC, APT, HEXRD, and TEM studies.

2.2   Metals Development Laboratory Efforts

Metallic glasses have been studied for several years at Metals Development Laboratory (MDL) of Metallurgical and Materials Engineering Department of Middle East Technical University. A great effort is made to understand the underlying mechanisms of anomalous nucleation of binary Al-RE marginal glass-

forming alloys upon devitrification. For this purpose, several experimental studies, supported by modeling and simulation, are performed. In this chapter, some of the many research studies conducted at MDL were briefly summarized and discussed.

In order to enlighten the outrageous nuclei density, which can reach up to 10^{24} m^{-3} in some marginal glass-forming systems, Demirtaş and Kalay [41] had investigated the crystallization kinetics of fcc-Al formation in the $Al_{90}Tb_{10}$ glass-forming system. The amorphous structure of as-spun ribbons is confirmed within the limits of TEM and XRD (Figure 2.1).
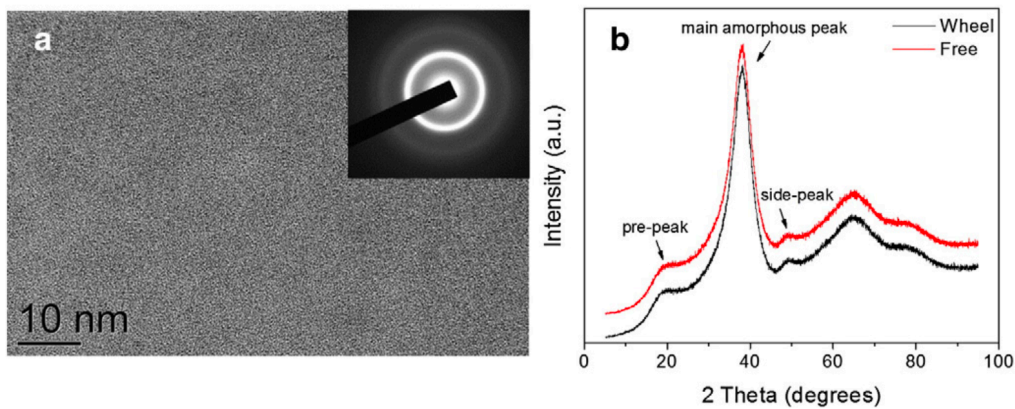
Figure 2.1 (a) HRTEM micrograph with SAED pattern (inset) and (b) XRD traces of as-spun $Al_{90}Tb_{10}$ ribbons (Adoptedf from [41])

Controlled crystallization of $Al_{90}Tb_{10}$ glassy alloy is performed by isothermal DSC heating. The amorphous samples are held at 220 ^{0}C, which is 16 ^{0}C lower than the T_x determined from the DSC scan of 40 ^{0}C/min heating rate. Figure 2.2 shows the BF-TEM images taken from different stages of the first crystallization event in the DSC scan. The nanocrystals are confirmed to be fcc-Al from the SAED and the XRD traces. When 20 different TEM images are evaluated, it is concluded that the fcc-Al nanocrystal population reaches up to 10^{21} m^{-3} for this composition. Previous FEM studies showed that there are fcc-like MRO structures inside the amorphous media [42]. These MRO structures were thought to be the main reason for the high density

16

of nuclei. The almost pure Al structures below sub-critical size might present in the structure and grow to be fcc-Al nanocrystals during isothermal heating. APT studies also revealed Al-rich regions in the amorphous ribbons of $Al_{90}Sm_{10}$, which are almost 1 nm in size [43]. However, whether these MRO structures are inherited from the liquid state or not is still inexplicit.
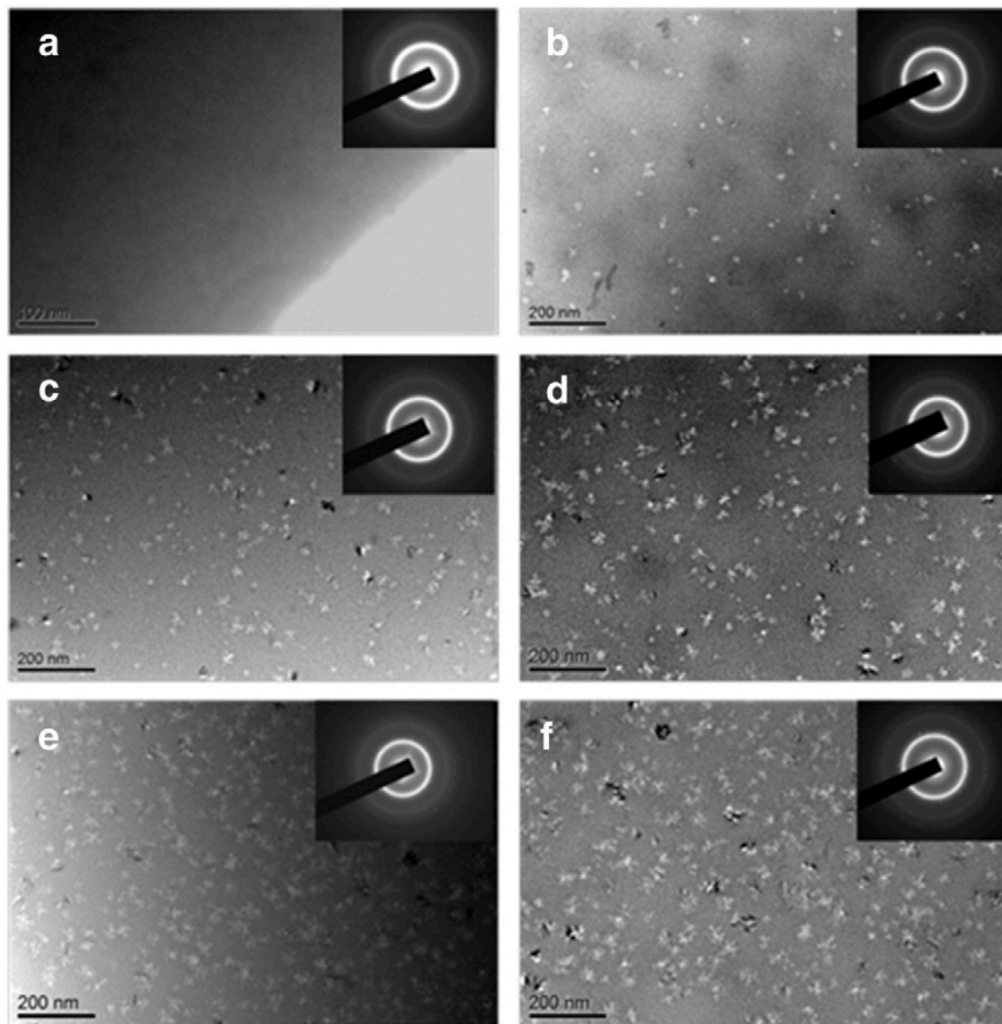
Figure 2.2 BF-TEM image and SAED pattern (inset) of (a) amorphous as-spun state and (b), (c), (d), (e), (f) fcc-Al nanocrystals at different stages of the isothermal heating curve (Adopted from [41])

Another study was conducted by Yıldırım et al. [44] further to investigate the fcc-like Al clusters within the amorphous state. In this study, the $Al_{90}Tb_{10}$ alloys are produced with both Cu block melt spinning and magnetron sputtering techniques. Initial structures of both samples are confirmed to be amorphous by HEXRD and TEM analyses. The glassy alloys are subjected to constant heating by DSC (Figure 2.3). Although the chemical compositions and the initial structures of the samples are the same, they had followed different crystallization pathways. In both cases, the first reactions belong to the fcc-Al formation, whereas the heat requirements are different for ribbons and thin films.
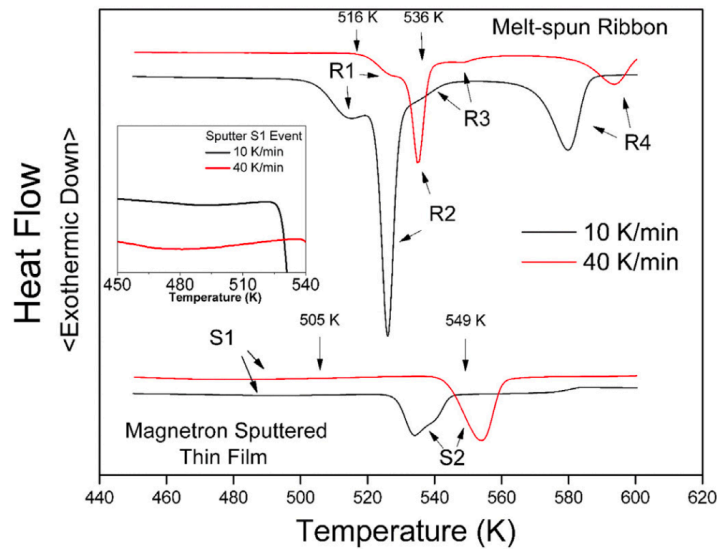
Figure 2.3 Constant heating DSC curves of $Al_{90}Tb_{10}$ melt-spun ribbons and magnetron sputtered thin films (Adopted from [44])

2D film plots are shown in Figure 2.4 also support the heat flow curves of DSC experiments. Upon heating, the melt-spun ribbons pass the fcc-Al region faster, and then the structure transforms into a hexagonal phase. However, this transformation is not seen for magnetron sputtered thin films. Since the samples are produced with different methods, the initial structures may not be the same. For the magnetron sputtering case, the cooling rate is 10^9 K/s, and the amorphous structure is originated from the vapor phase. On the other hand, the cooling rate is 10^6 K/s for the melt-spun ribbons, and the structure is quenched from the liquid phase. These findings support

18

the previous hypothesis. The MRO fcc-like Al clusters may be inherited from the liquid state and act as pre-existing nuclei during devitrification. However, they are not observed in the vapor phase quenching process.
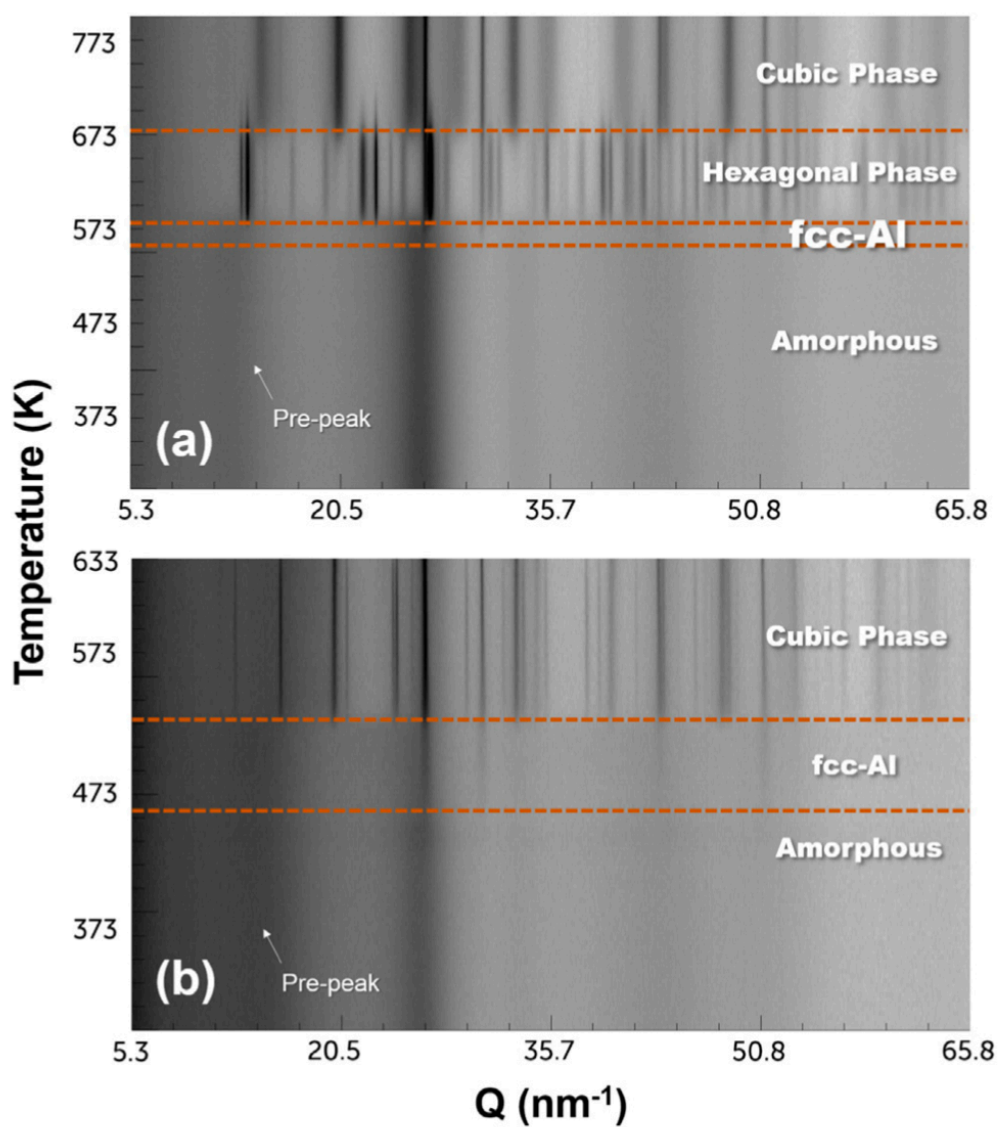
Figure 2.4 2D film plots of in-situ HEXRD traces of (a) melt-spun ribbons and (b) magnetron sputtered thin films of $Al_{90}Tb_{10}$ alloys (Adopted from [44])

Many studies concluded that the MRO fcc-like structures, and therefore anomalous nucleation density upon devitrification, should be originated from the liquid state, and the amorphous state is not so homogenous after all. However, it is difficult to investigate the molten state and analyze tiny features of few nanometers using conventional characterization tools. Therefore, it is crucial to support the experimental findings with simulation and modeling data for interpretation in such cases.

Övün et al. [45] computed structural modeling of liquid and amorphous states by Monte Carlo (MC) simulations in the $Al_{91}Tb_9$ system. The experimental HEXRD data is used to calculate the interatomic potentials. According to Warren-Cowley, Voronoi Tessellation and SRO analysis resulted in pure Al clusters that led to compositional inhomogeneity. Figure 2.5 (a) shows the change in cluster size and the fraction of Al atoms in clusters with respect to decreasing temperature. Due to kinetic restrictions, the Al regions stop growing below 600 ^0C, which is the glass transition temperature (T_g). Figure 2.5 (b)-(e) demonstrates the spatial distribution of clusters. The size distribution of clusters is also shown by color codes. The study concluded that the pure Al clusters trapped in the amorphous state and isolated from each other could be the reason for extreme nucleation upon crystallization. These inhomogeneities found by MC simulations in the nanoscale also correlate with the previous APT results [42].
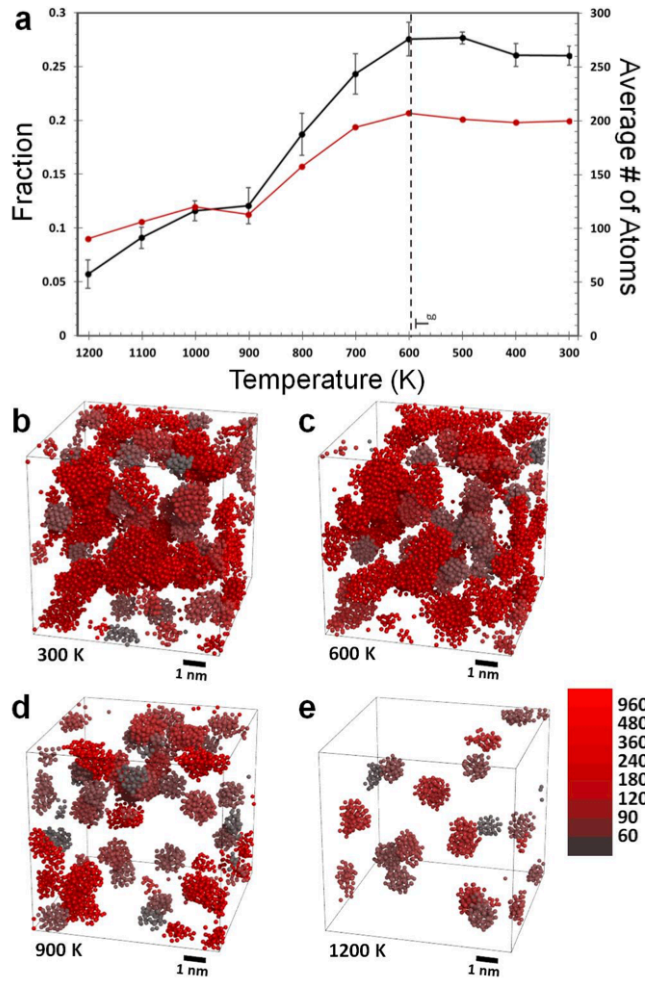
Figure 2.5 (a) Al atom fraction of pure Al clusters (black) and cluster size (red). (b)-(e) Spatial distribution of Al clusters at different temperatures (Adopted from [45])

As mentioned in the previous section, Yıldırım et al. was experimentally investigated the structural changes in two different binary metallic glass samples having the exact composition of $Al_{90}Tb_{10}$ but produced by different methods, which were in the form of ribbons produced by melt-spinning and thin films produced by DC magnetron sputtering technique. Additionally, Kutsal [46] proceeded with Reverse Monte Carlo simulations to the Yıldırım's experimental synchrotron X-Ray diffraction and FEM data. So, short-range and medium-range scale topologies were examined for both

glassy alloys by carrying out numerical analysis to calculate total X-ray structure factor and pair distribution functions.

Experimentally collected HEXRD data were processed to calculate total structure function S(Q) by eliminating side effects. It is also essential for the pair distribution function (PDF) since it is expressed as the Fourier transform of S(Q). While pair-pair correlations can be understood by S(Q), how atoms exhibit such orientations with respect to bond length, coordination number, and bonding behaviors is simulated by the pair distribution function. The calculated average bond orientation angles as a result of RMC simulations are shown in Table 2.1. Except for Tb-Tb-Tb, all other atomic bonding exhibit similar angle orientations. Nevertheless, Tb-Tb-Tb is strictly the same for both samples [46].

Table 2.1 Bond orientation angle calculations of $Al_{90}Tb_{10}$ system produced by different methods [46]

	Al-Al-Al	Al-Tb-Al	Tb-Al-Tb	Tb-Al-Al	Tb-Tb-Al	Tb-Tb-Tb
Melt-Spun Ribbon	61.8	53.3	67.5	64.6	56.7	60.1
Magnetron Sputtered Thin Film	62.1	53.0	67.9	65.2	56.6	60.1

Moreover, considering RMC and ECP model, the calculated local coordination number for both alloys is shown in Table 2.2.

Table 2.2 Local average coordination number of $Al_{90}Tb_{10}$ binary glass growth using two techniques concerning the RMC and ECP simulations [46]

	Al-centered	Tb-centered
Melt-Spun Ribbon	14	15
Magnetron Sputtered Thin Film	14	15
ECP Model	13.08	17

Structural analyses of melt-spun ribbon and magnetron sputtered $Al_{90}Tb_{10}$ thin films were conducted in detail. As a result of RMC simulations, both compositions exhibit similar properties for short-range order. However, with respect to medium-range order, they are different from each other, and FEM studies also support this outcome.

Kutsal successfully demonstrated the simulation of the $Al_{90}Tb_{10}$ glass-forming system in the form of a melt-spun ribbon and magnetron-sputtered thin film by RMC simulations based on experimental HEXRD data. However, sometimes a simulation model may fit more than one real system. Therefore, it is essential to make some restrictions on the simulation by giving more experimental input data. Ulucan [47] conducted another RMC simulation study on the same binary system. This time, in addition to HEXRD experiments, extended X-ray absorption fine structure EXAFS measurements are also considered.

RMC simulations can model the atomic configuration of amorphous materials in 1D or 3D configurations. If only S(Q) data is considered, RMC simulations show 1D structural results that exhibit similar behavior with the XRD data. However, 3D local atomic orientation can be obtained by the implementation of EXAFS data. In this study, pure aluminum clusters were modeled by RMC. For this reason, all Tb atoms and their first shell neighbors were not considered. This means that only Al-Al contacts were investigated. Also, the five most prominent clusters were taken into account during simulations shown in Figure 2.6.

The simulations showed that melt-spun $Al_{90}Tb_{10}$ ribbons have a higher degree of order compared to the magnetron-sputtered thin films. The Voronoi analysis also shows that the cluster size of Al in thin-film specimens is smaller than the ribbon, and their clusters were not collected. Moreover, it was found in both simulation techniques that fcc-Al cluster size in unit volume is higher in ribbon samples than sputtered samples.
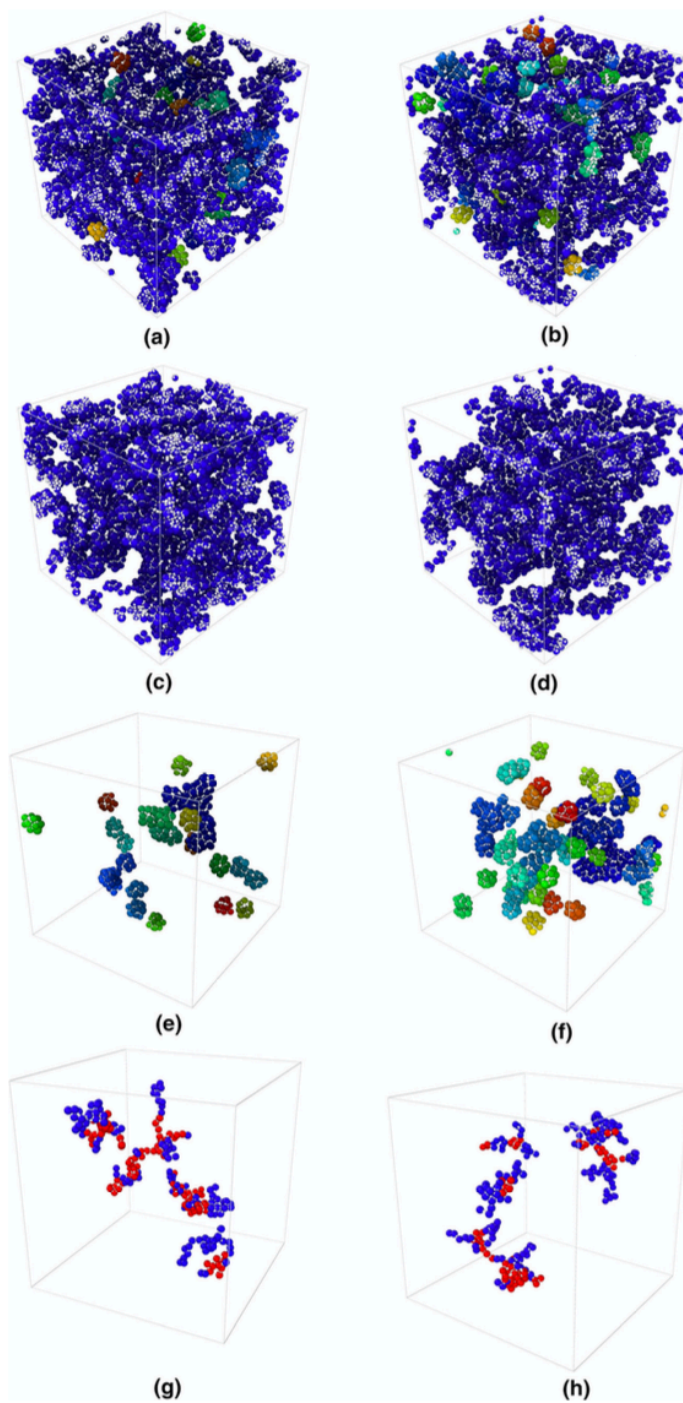
Figure 2.6 Simulation results of melt-spun ribbon and magnetron sputtered $Al_{90}Tb_{10}$ compositions concerning the Voronoi Cell, Network, Separate, and Pure Al clusters simultaneously (Adopted from [47])

2.3 Experimental Procedure

2.3.1 Production of Alloys

Ingots of $Al_{90}Sm_5Tb_5$ and $Al_{90}Y_5Tb_5$ are prepared by electric arc melting under argon atmosphere from highly pure elements and remelted several times to obtain high chemical homogeneity. Amorphous ribbons of 1-3 mm width and 20-30 μm thickness are produced by a single Cu block melt spinner with 30m/s tangential speed under 1/3 atm helium atmosphere. All samples are prepared at Ames Laboratory, USA. Melt-spun ribbons are shown in Figure 2.7. The composition of as-spun ribbons is affirmed by electron microprobe analysis.
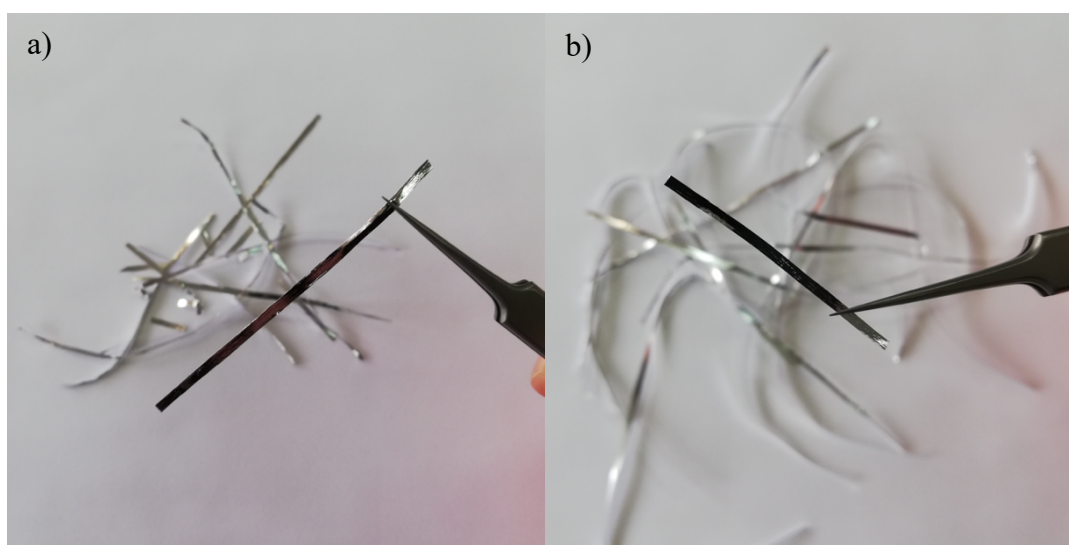
Figure 2.7 Melt-spun ribbons of (a) $Al_{90}Sm_5Tb$ and (b) $Al_{90}Y_5Tb_5$ alloys

2.3.2 Differential Scanning Calorimetry Analysis

Differential scanning calorimetry (DSC) experiments are performed by using Q2000 equipment of TA Instruments brand. In Figure 2.8, a representative image of the Q2000 system is shown. Melt spun ribbons of $Al_{90}Sm_5Tb_5$ and $Al_{90}Y_5Tb_5$ compositions are cut into small pieces, and 5 mg of each sample is directly put into

aluminum pans without any preprocessing. Aluminum pans are enclosed with aluminum lids and pressed to seal. The study is carried out under a protective helium atmosphere at a 25 mL/min gas flow rate. Samples are heated between 300-673 K at a constant heating rate of 10 K/min and then cooled down to room temperature. During all the experiments, an empty sealed aluminum pan is used as the reference sample.

Figure 2.8 TA Instruments Q2000 DSC equipment (Adopted from [48])

2.3.3 High Energy X-Ray Diffraction Analysis

The high-energy X-Ray diffraction analyses of $Al_{90}Sm_5Tb_5$ and $Al_{90}Y_5Tb_5$ samples were carried out at BL-04 MSPD beamline in ALBA synchrotron light source, Spain (Figure 2.9). During the experiments, the wavelength of the incoming X-ray beam was set to 0.496Å by a double Si monochromator with 25 keV energy. Both samples were prepared inside pyrex capillary tubes. As-spun ribbons of $Al_{90}Sm_5Tb_5$ and $Al_{90}Y_5Tb_5$ were cut into small pieces and put inside glass capillaries with 1 mm diameter and 0.01 mm wall thickness. Then, the capillary tubes were vacuumed and

sealed under Ar atmosphere. Room temperature data were collected from these samples with 3 second exposure times using a Mythen array detector system. An empty sealed pyrex capillary tube was exposed with the same parameters, and the collected data was used for background correction. Since the samples were not free-standing and the exposure time was short, the collected room temperature data were noisy. Therefore, these data sets are normalized using the simple moving average (SMA) statistical method, and the moving window size is set to 60. In order to prevent the shifting of peak positions, center moving average analysis is computed.
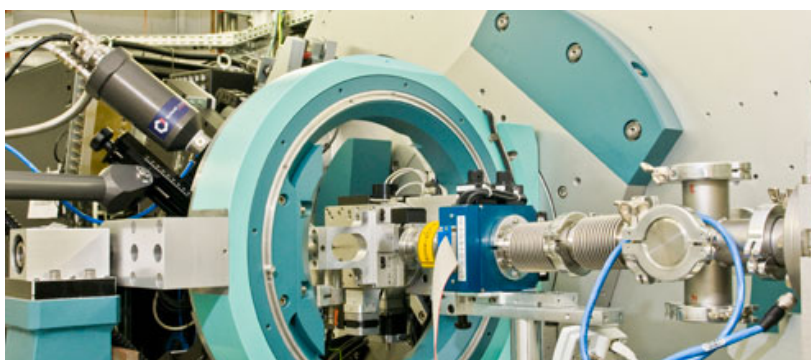
Figure 2.9 BL-04 MSPD beamline in ALBA synchrotron light source (Adopted from [49])

In-situ high-temperature HEXRD data is collected from room temperature to 773K with a 10K/min heating rate using a hot air blower. The system's temperature is measured with thermocouples placed near the exit of the air blower having 2K temperature tolerance. A total of 290 XRD patterns are collected from each sample and the 2D film plots of diffraction data are prepared by Powder3D software [50].

HEXRD data are collected in 0.4 - 9 Å^{-1} Q range where θ is the Bragg's angle and λ is the wavelength of the incoming X-ray beam in the following Equation 2.1

$$Q = \frac{4\pi \sin\theta}{\lambda}$$ Eq. 2.1

All data, including room-temperature measurements and the in-situ high-temperature experiments, are corrected for background, polarization, absorption, multiple, and Compton scattering. Total structure factor function S(Q) is calculated using the following Equation 2.2, where $I^c(Q)$ is the coherent scattering intensity normalized to a_i, atomic concentrations, and $f_i(Q)$ is the atomic scattering factors for each different element in the system. [51]

$$S(Q) = 1 + \frac{I^c(Q) - \sum_{i=1}^{n} a_i |f_i(Q)|^2}{\left| \sum_{i=1}^{n} a_i f_i(Q) \right|^2} \qquad \text{Eq. 2.2}$$

2.3.4 Transmission Electron Microscopy Analysis and Sample Preparation

Transmission electron microscopy (TEM) samples are prepared by focused ion beam (FIB) at Bilkent University National Nanotechnology Research Center (UNAM). In Figure 2.10, FIB sample preparation steps are shown for the as-spun ribbon sample of $Al_{90}Sm_5Tb_5$, respectively. There are four fundamental steps of sample preparation by FIB as follows. At the first step, the region of interest on the sample is coated with a sacrificial platinum layer to protect the sample during ion milling (Figure 2.10 (a)). Second, the backside and the front side of the sample are ion milled to approximately 10 μm in depth (Figure 2.10 (b)). The milling process continues until only one side of the lamella is remained in contact. After this step, the lamella is ready for extraction (Figure 2.10 (c)). The lamella is Pt welded to the omniprobe from the free end at the third step of the sample preparation procedure. The unetched side which was still in contact is etched, and the sample is extracted onto the omniprobe. Then, the sample is Pt welded onto the TEM grid, and the omniprobe is released (Figure 2.10 (d)). At the final step, the sample is thinned to the desired thickness so that electrons can pass through during TEM analyses (Figure 2.10 (e)). Figure 2.10 (f) shows the distant view of the prepared TEM sample on the grid.
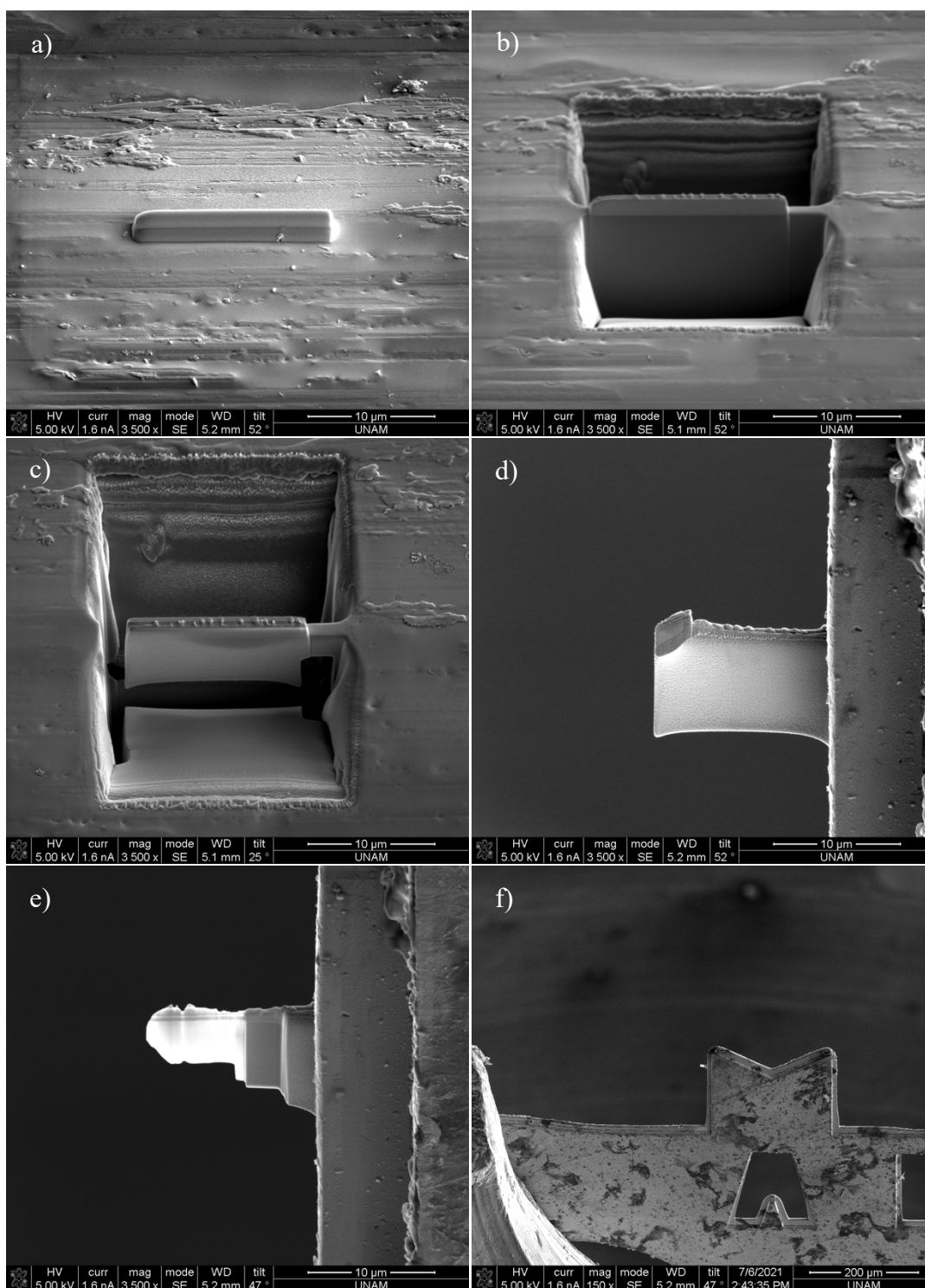
Figure 2.10 SEM micrographs of Al$_{90}$Sm$_5$Tb$_5$ as-spun TEM sample preparation steps by FIB

TEM analyses are done at METU Central Laboratory using JEOL JEM2100F scanning/transmission electron microscope operating at 200 kV accelerating voltage. The microscope used in this study is shown in Figure 2.11.

Figure 2.11 JEOL2100F transmission electron microscope at METU Central Laboratory

2.3.5 Atom Probe Tomography Analysis and Sample Preparation

Melt spun ribbons of amorphous $Al_{90}Sm_5Tb_5$, and $Al_{90}Y_5Tb_5$ samples are heated by Q2000 DSC equipment until the peak temperature of their first crystallization reaction and then rapidly cooled down to room temperature by liquid nitrogen to interrupt the reaction. The heating experiments are conducted under a protective He atmosphere to prevent oxidation. Then, atom probe tomography (APT) samples are prepared using heat-treated ribbons by FIB at Microscopy and Characterization Center of Center for Advanced Energy Studies (CAES) in Idaho, USA, with the valuable help of Dr. Yaqiao Wu. The APT sample preparation procedure is similar to the TEM sample preparation, but there is one extra step. After the extraction, the sample is mounted onto stainless steel needle by platinum welding, and then it is sharpened by Ga^+ ion etching. The etching process continues

30

until a sharp tip with a curvature radius of less than 50 μm is formed. A significant amount of gallium atoms is penetrated inside the sample and revealed in APT analyses. In Figure 2.12, the gallium atom distribution in the APT results of $Al_{90}Y_5Tb_5$ and the SEM image of the prepared sample tip are shown, respectively.
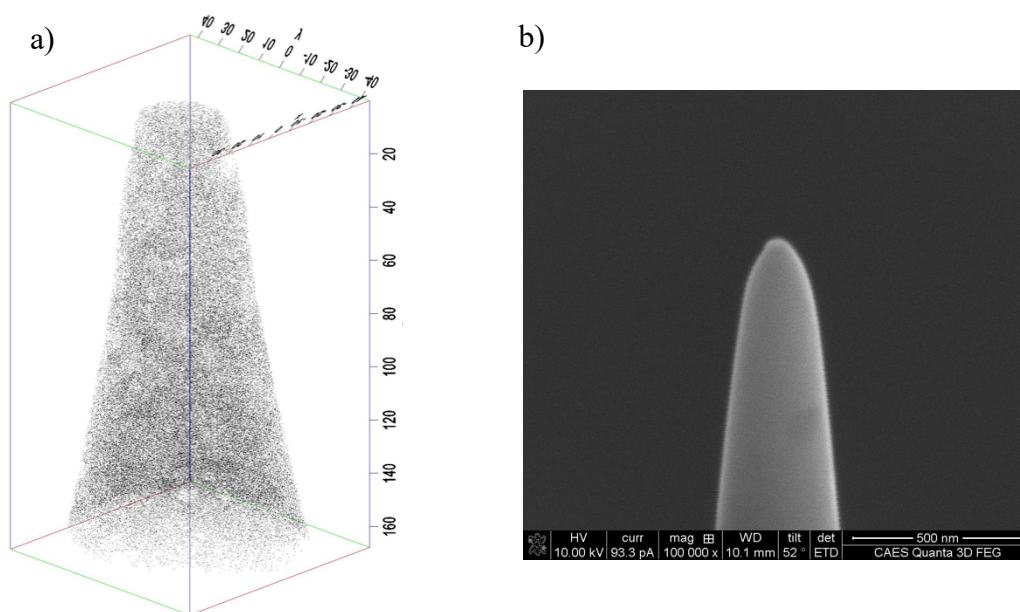
Figure 2.12 (a) Gallium atom distribution and (b) SEM image of the sample tip

APT experiments are carried out by IMAGO Local Electron Atom Probe (LEAP) equipment at Idaho National Laboratory, Center of Advanced Energy Studies (CAES) in Idaho, USA. Samples of $Al_{90}Sm_5Tb_5$ and $Al_{90}Y_5Tb_5$ are examined in both laser pulse mode and voltage pulse mode. Laser pulsed APT experiments are conducted at a pulse energy of 50 pJ, pulse rate of 200 kHz, and a detection rate of 0.5-1%. Voltage pulsed APT experiments are conducted at a pulse rate of 200 kHz, pulse fraction of 20%, and detection rate of 2%. Temperature is set to 50K for all experiments. The experimental data are analyzed using IVAS LT software. The IMAGO LEAP instrument used in this study is shown in Figure 2.13.
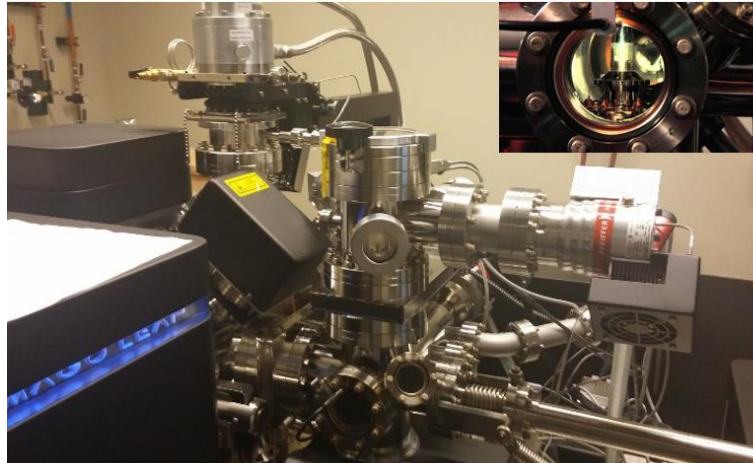
Figure 2.13 IMAGO LEAP instrument located at Idaho National Laboratory
(Adopted from [52])

2.4   Results and Discussion

2.4.1   The Amorphous State and Composition of Melt Spun Ribbons

Compositional homogeneity of melt-spun ribbons is investigated by electron probe micro-analyzer (EPMA) and EDS/SEM.   Representative samples are taken from $Al_{90}Y_5Tb_5$ and $Al_{90}Sm_5Tb_5$ as-spun ribbons and subjected to energy dispersive X-ray spectroscopy (EDS) and wavelength dispersive X-Ray spectroscopy (WDS) analyses. Results are tabulated in Table 2.3. According to WDS and EDS results, the chemical homogeneities of samples are considered adequate for this study. As previously mentioned in section 2.3.1, the ingots of each composition are remelted several times during production with arc melting to provide high chemical homogeneity.

Table 2.3 Composition determination by EDX/SEM

$Al_{90}Y_5Tb_5$ as-spun ribbon			$Al_{90}Sm_5Tb_5$ as-spun ribbon		
Al (at %)	Y (at %)	Tb (at %)	Al (at %)	Sm (at %)	Tb (at %)
89.44	5.14	5.42	89.75	5.44	4.82
89.76	4.80	5.44	89.79	5.24	4.87
89.35	5.20	5.43	89.94	5.19	4.88
89.75	4.82	5.43	90.14	4.88	4.99
89.76	4.72	5.52	90.16	5.09	4.75

As-spun ribbons are subjected to HEXRD analysis, and corresponding room temperature plots are given in Figure 2.14. HEXRD results are indicated amorphous structures for both $Al_{90}Y_5Tb_5$ and $Al_{90}Sm_5Tb_5$ compositions in as-spun states. In addition to the main amorphous peak, there are also a pre-peak and a side-peak for both samples, which are characteristics of Al-RE based marginal metallic glasses. In Figure 2.14, as-spun HEXRD plots of $Al_{90}Tb_{10}$, $Al_{90}Sm_{10,}$ and $Al_{90}Y_{10}$ marginal metallic glass alloys are also present for comparison with ternary alloys. The mystery of pre-peak and side peaks in the XRD trace is still not solved, but the RE elements in marginal metallic glasses are responsible for this phenomenon. Y element is known to exhibit low scattering compared to other RE elements such as Sm or Tb, and the HEXRD pattern of $Al_{90}Y_{10}$ does not show any sign of a side peak. Hence, the disappearance of the side peak and the low pre-peak intensity in the HEXRD trace of $Al_{90}Y_{10}$ composition supports the hypothesis. In Table 2.4, pre-peak, main amorphous peak, and side peak positions are tabulated for each composition.

Table 2.4 Pre-peak, main amorphous peak and side-peak positions for as-spun conditions of binary and ternary alloys

Composition	Pre-peak ($\mathring{A}^{-1}$)	Main amorphous peak ($\mathring{A}^{-1}$)	Side peak ($\mathring{A}^{-1}$)
$Al_{90}Y_5Tb$	1.32	2.64	3.40
$Al_{90}Sm_5Tb_5$	1.36	2.63	3.43
$Al_{90}Tb_{10}$	1.33	2.63	3.40
$Al_{90}Sm_{10}$	1.28	2.63	3.37
$Al_{90}Y_{10}$	1.47	2.66	-
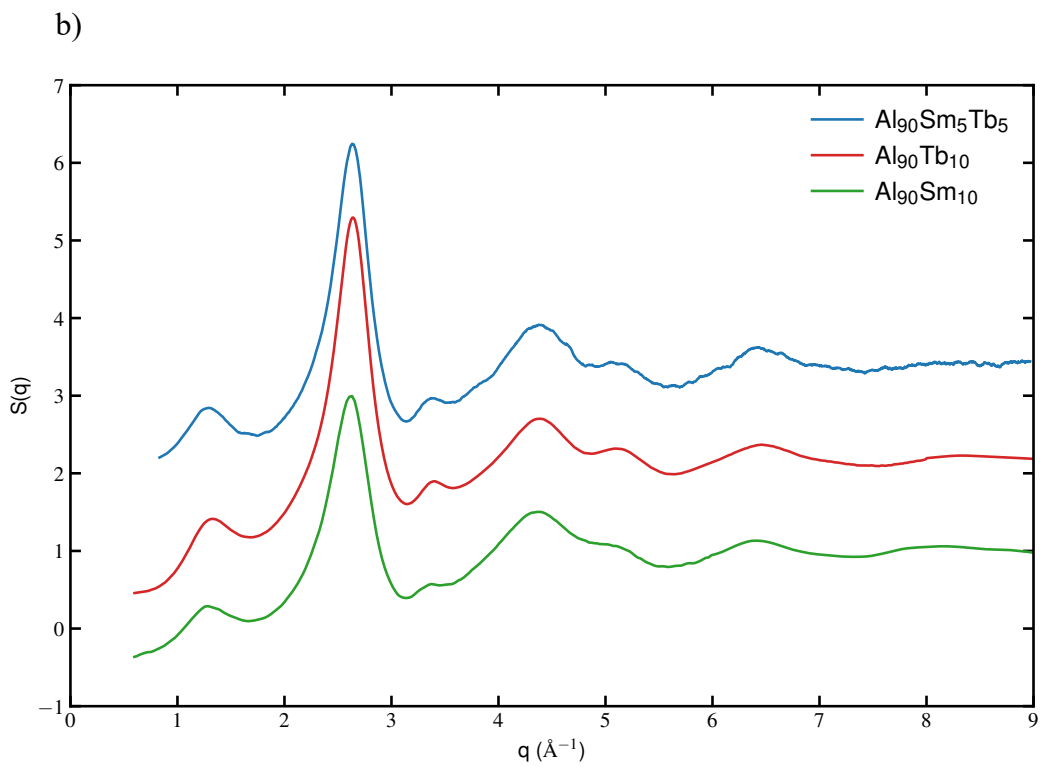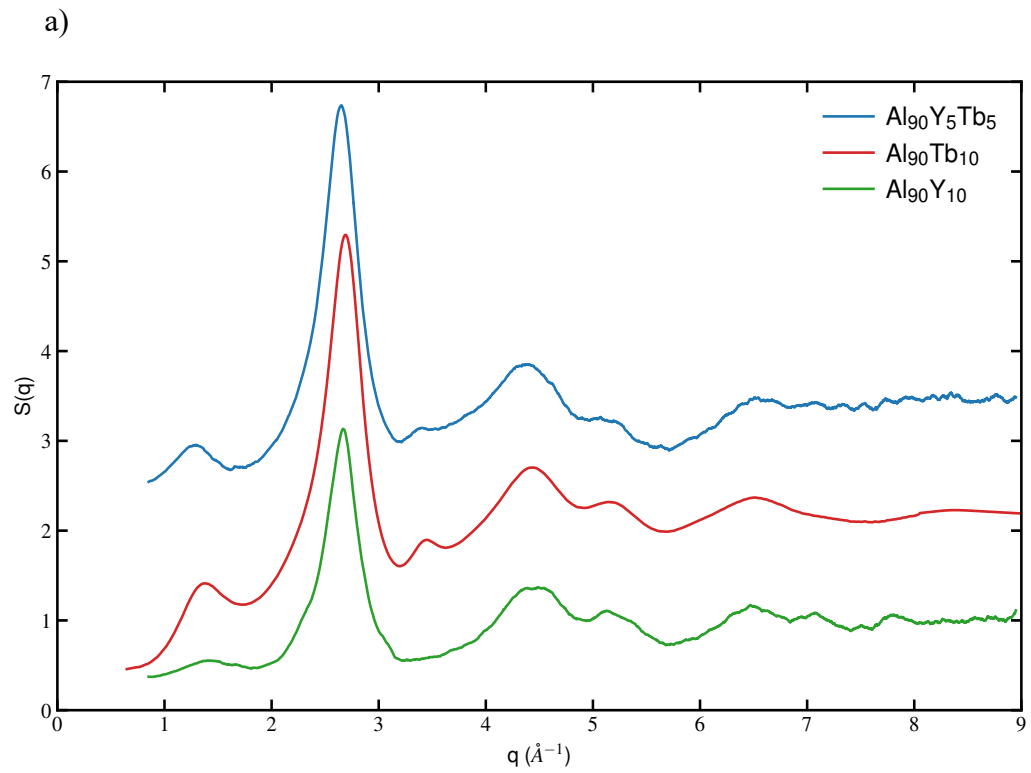
Figure 2.14 HEXRD plots of $Al_{90}T_5Tb_5$ and $Al_{90}Sm_5Tb_5$ melt-spun ribbons and corresponding binary alloys at room temperature

For the final investigation of the as-spun state, the structures are analyzed by TEM. In Figure 2.15, the bright-field TEM micrographs and corresponding selected area electron diffraction (SAED) patterns of as-spun $Al_{90}Sm_5Tb_5$ and $Al_{90}Y_5Tb_5$ are shown. Within the limits of TEM and HEXRD, the ribbons of both compositions brought out fully amorphous structures in their as-spun states.
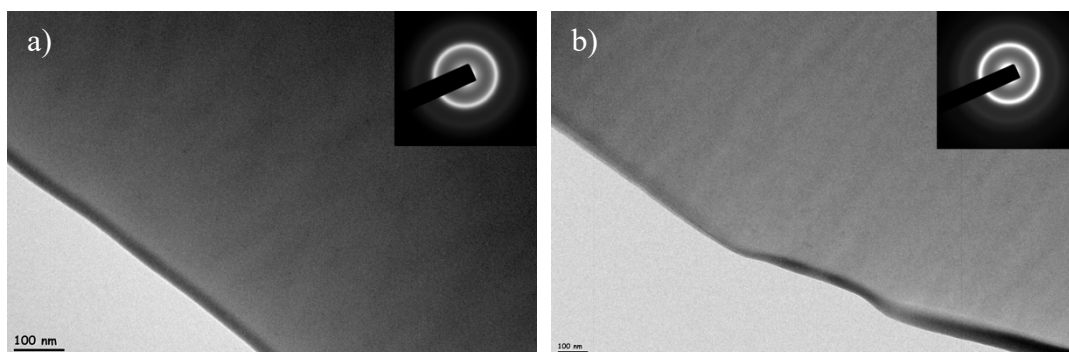
Figure 2.15 Bright-field TEM micrographs and corresponding SAED patterns (inset) of as-spun (a) $Al_{90}Sm_5Tb_5$ and (b) $Al_{90}Y_5Tb_5$ ribbons

2.4.2 Controlled Devitrification Study of $Al_{90}Y_5Tb_5$ and $Al_{90}Sm_5Tb_5$ Glassy Alloys

Amorphous ribbons are heated from room temperature to 650K by DSC with a 10K/min heating rate, and the resulting traces are shown in Figure 2.16. Both compositions of $Al_{90}Y_5Tb_5$ and $Al_{90}Sm_5Tb_5$ did not show any definite endothermic transformation belonging to glass transition before the first exothermic crystallization reaction. Most of the time, Al-based marginal glass formers do not show a separate glass transition signal on DSC trace since the glass transition temperature (T_g) intersects with the onset temperature of the first crystallization peak (T_x) [41], [42].

The first crystallization event is the main difference between the two compositions. Previous studies show that the first reaction belongs to fcc-Al nanocrystal formation during the devitrification of Al-RE-based binary marginal metallic glasses. In this reaction, the ultra-high density of fcc-Al nanocrystals form in the amorphous matrix, and this nanocrystal formation is come out as a low-intensity broad peak in the DSC trace [41], [44], [46]. When the DSC results of $Al_{90}Y_5Tb_5$ are analyzed, the first exothermic reaction, which belongs to Al nanocrystal formation, is consistent with the literature. However, the DSC trace of $Al_{90}Sm_5Tb_5$ reveals a different trend. In this trend, the expected broad peak of the Al nanocrystal formation is not seen; only two sharp peaks exist. This distinction between two Al-based marginal glass alloys is further discussed with HEXRD, TEM, and APT analyses.
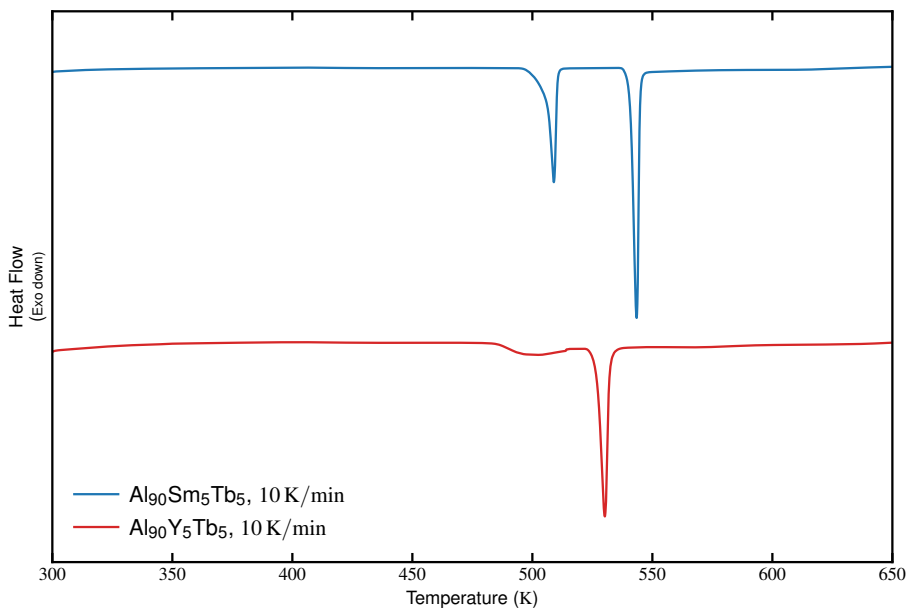
Figure 2.16 DSC traces of $Al_{90}Y_5Tb_5$ and $Al_{90}Sm_5Tb_5$ from room temperature to 650K

Another controlled devitrification experiment was held at the ALBA synchrotron light source by Prof. Dr. Y. Eren Kalay and previous group member Mustafacan Kutsal [46]. Amorphous ribbons are heated from room temperature to 773K, and in-situ HEXRD data is collected. During the devitrification experiment, 290 XRD data

for each composition are collected. The 2D film plots of these data sets are shown in Figure 2.17. When the HEXRD traces of $Al_{90}Y_5Tb_5$ are analyzed, three consecutive reactions occur. Since the temperature range of the fcc-Al nanocrystallization reaction is wide, a single reaction temperature cannot be determined from DSC or HEXRD. However, the average temperature can be taken as 490 K from the HEXRD data. The second and third transformations occur approximately at 531 K and 688 K. The reaction temperatures determined by HEXRD are consistent with the temperature data obtained from exothermic DSC peaks. Since the heating rate is 10 K/min for both controlled devitrification experiments, it is expected to get the supporting results. However, the third reaction could not be determined by DSC as the reaction temperature is out of scanning range.

In the first reaction of the $Al_{90}Y_5Tb_5$ system, the formation of FCC Al nanocrystals occurs as expected from Al-RE-based marginal metallic glasses. It is believed that after the second and third reactions, the structure consists of an Al matrix and two or more intermetallic compounds of Al, Y, and Tb. However, when the XRD traces of $Al_{90}Sm_5Tb_5$ are examined, no phase transformation that belongs mainly to Al nanocrystal formation from the amorphous structure was found. Approximately at 503 K, two or more intermetallic compound formations simultaneously occur as the fcc-Al nanocrystal formation, and at 546 K, a second phase transformation takes place. Figure 2.18 demonstrates XRD plots for selected temperatures from in-situ heating HEXRD experiments.

a)

b)
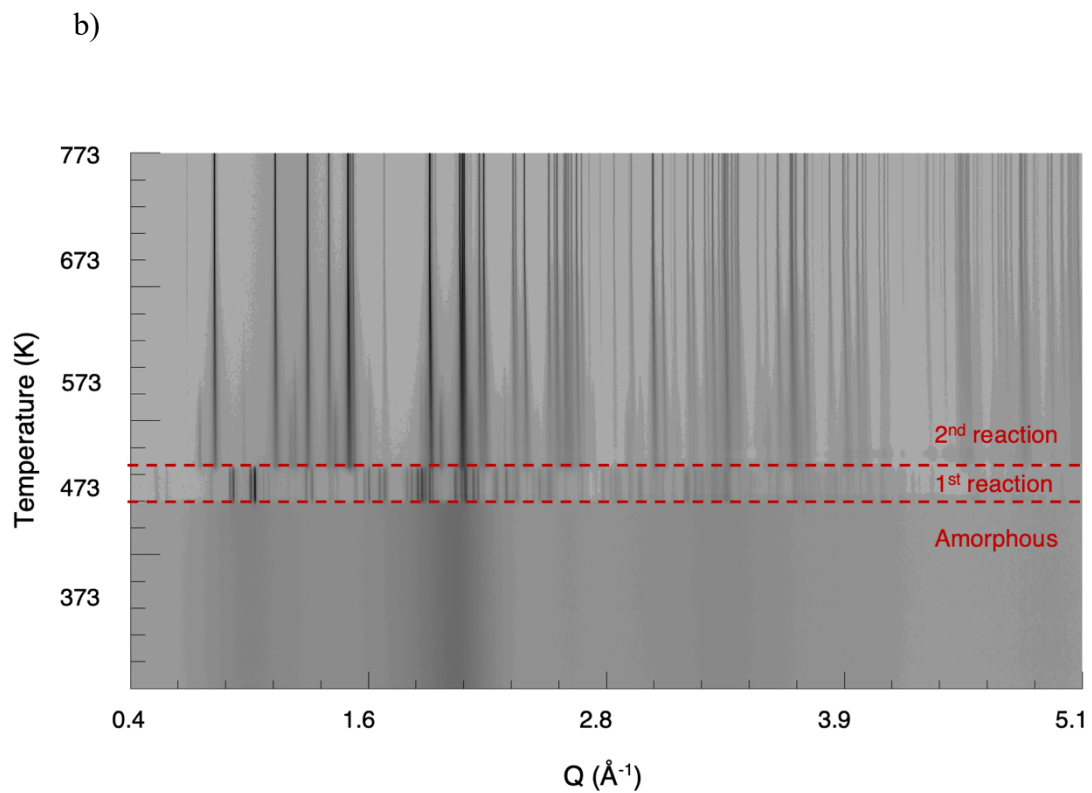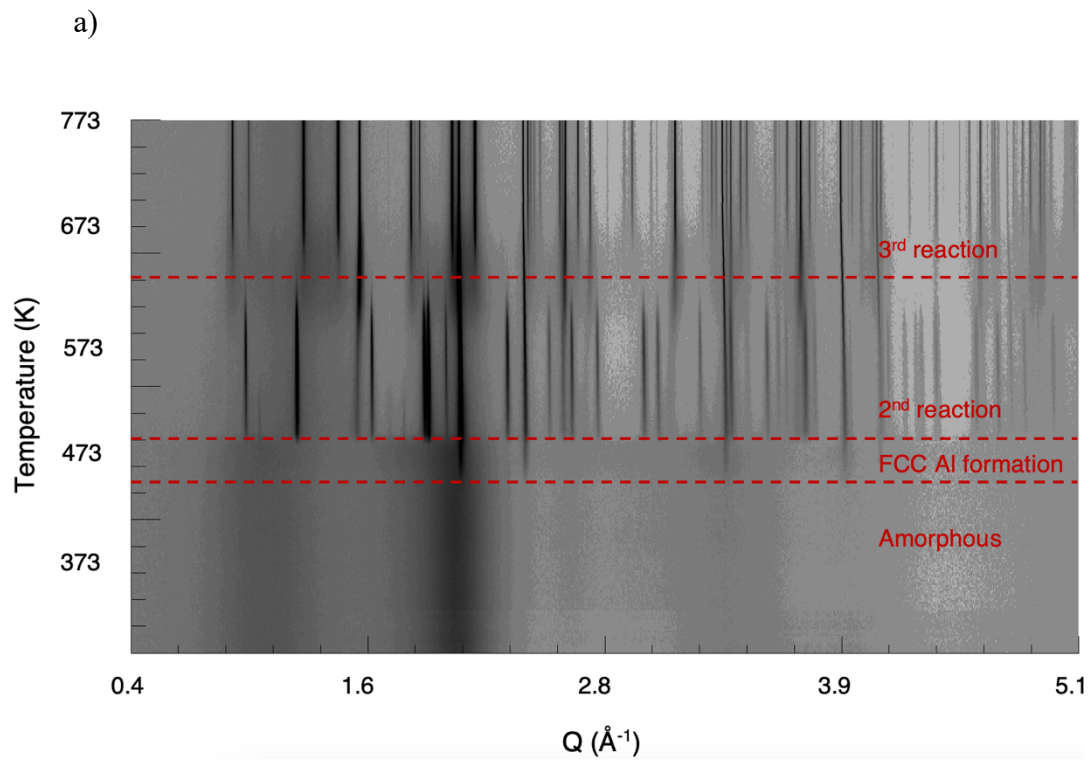
Figure 2.17 2D film plots of in-situ heating HEXRD analyses of a) $Al_{90}Y_5Tb_5$ and b) $Al_{90}Sm_5Tb_5$ compositions (Adopted from [46])
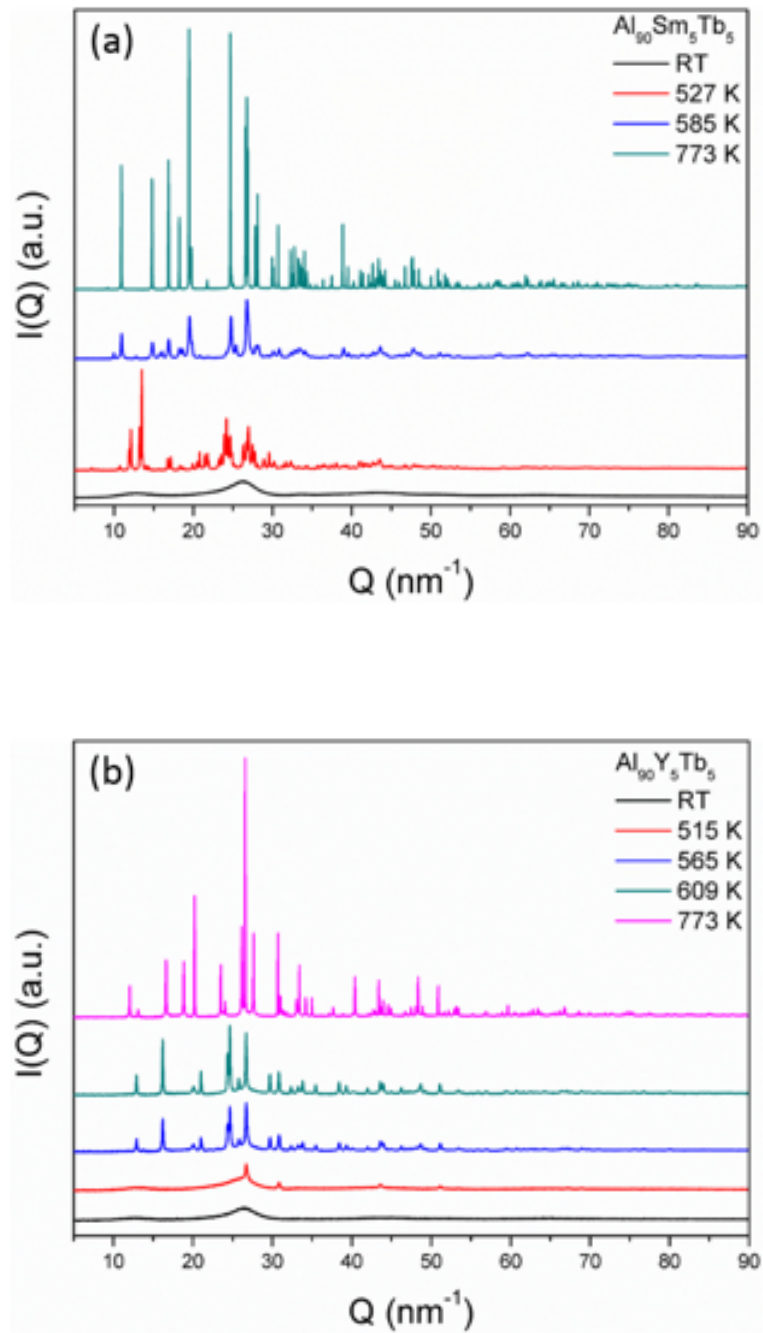
Figure 2.18 XRD plots of selected temperatures from in-situ heating HEXRD data set a) $Al_{90}Sm_5Tb_5$ and b) $Al_{90}Y_5Tb_5$ (Adopted from [46])

2.4.3 Investigation of First Exothermic Reaction Upon Crystallization

2.4.3.1 Transmission Electron Microscopy Results

HEXRD results presented in Figures 2.17 and 2.18 showed that during the first reaction upon crystallization of $Al_{90}Y_5Tb_5$ glassy alloy, fcc-Al nanocrystal formation in the amorphous matrix is similar to Al-RE binary systems. However, HEXRD analysis could not specify the density, size, and morphology of these nanocrystals. For these purposes, TEM and APT analyses are conducted. In Figure 2.19, BF TEM micrographs and corresponding SAED patterns are presented for $Al_{90}Y_5Tb_5$ composition. Since the first exothermic reaction is interrupted by rapid cooling, a significant amount of amorphous ternary alloy is still present in the structure. Hence, a dominant halo belonging to the amorphous matrix is seen in the corresponding SAED pattern. In addition, many nanoparticles are observed on the amorphous matrix, and these nanoparticles in the micrographs are proved to be fcc-Al nanocrystals from the SAED pattern.

Figure 2.19 BF TEM micrographs and corresponding SAED patterns (inset) of $Al_{90}Y_5Tb_5$ belonging to the interrupted first reaction

The TEM micrographs of the $Al_{90}Sm_5Tb_5$ sample indicate different features when compared to the $Al_{90}Y_5Tb_5$ structure. From the HEXRD data demonstrated in Figures 2.17 and 2.18, it was known that upon the devitrification of $Al_{90}Sm_5Tb_5$ glassy alloy,

there is no single reaction that solely belongs to fcc-Al nanocrystal formation. Instead, one or more different phases evolve simultaneously with the fcc-Al nanocrystal formation. The findings of TEM analyses also support this outcome. BF TEM micrographs and corresponding SAED patterns in Figure 2.20 resulted in a very few amount of parent phase (amorphous), tiny fcc-Al nanocrystals, and unidentified crystal phases. Both samples of $Al_{90}Sm_5Tb_5$ and $Al_{90}Y_5Tb_5$ are prepared by interrupting the first crystallization event after T_x, but the retained primary phase amounts are different. This phenomenon is due to the differences in reaction kinetics. It is possible to surmise by evaluating the shape or position of the reaction peaks to some degree. In DSC, sharper peaks mean faster transformation rates [53]. Therefore, it could be concluded that the decomposition of the amorphous phase in $Al_{90}Sm_5Tb_5$ occurs faster than $Al_{90}Y_5Tb_5$. A closer perspective of BF TEM of $Al_{90}Sm_5Tb_5$ and an HRTEM image is given in Figure 2.21, and Figure 2.22, respectively, and the possible fcc-Al nanocrystals are indicated.
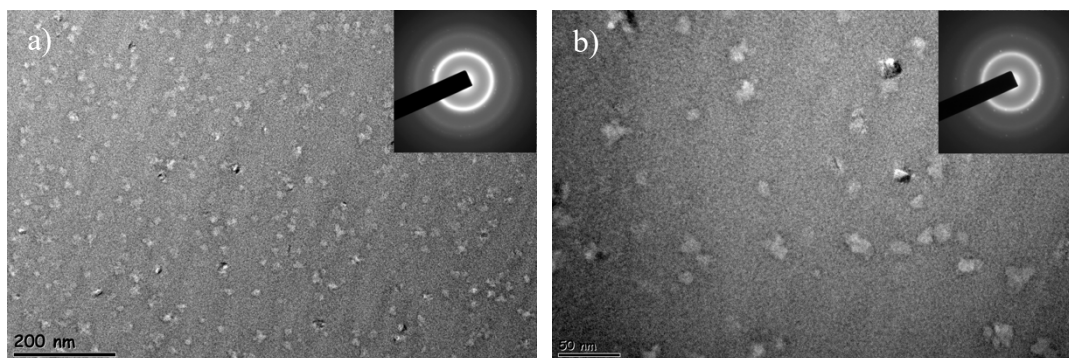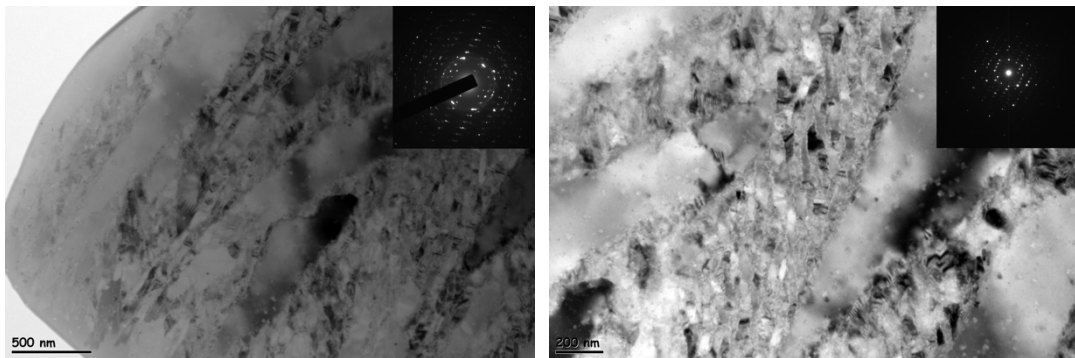

Figure 2.20 BF TEM micrographs and corresponding SAED patterns (inset) of $Al_{90}Sm_5Tb_5$ belonging to the interrupted first reaction
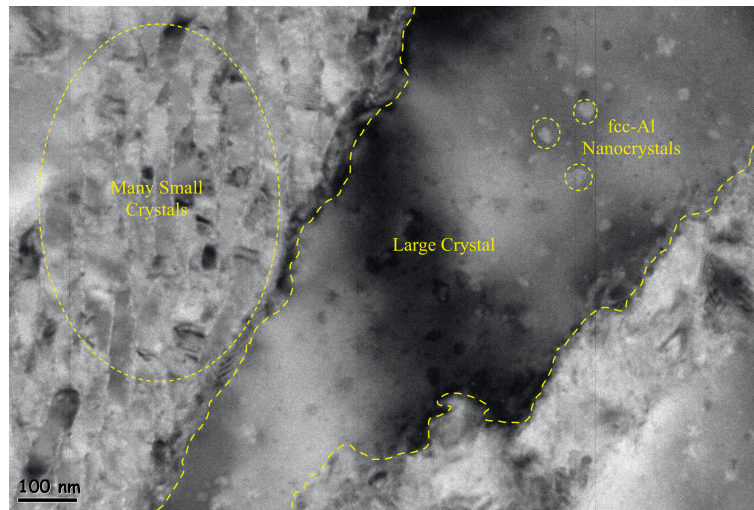
Figure 2.21 BF TEM micrograph of $Al_{90}Sm_5Tb_5$ indicating the different phases
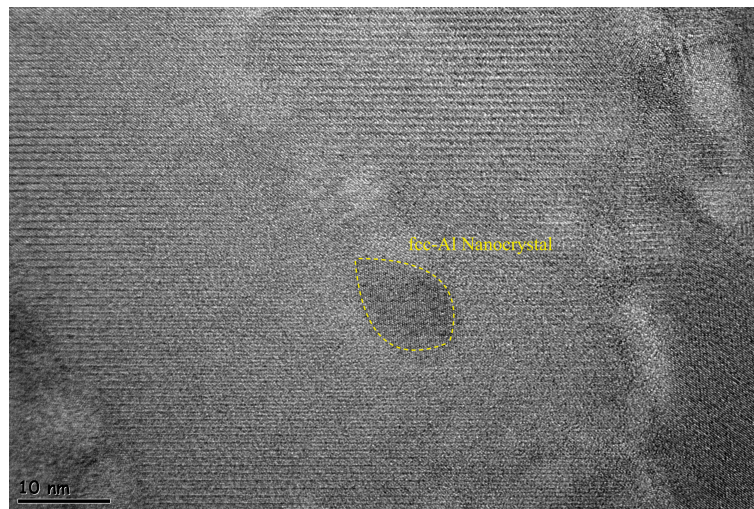
Figure 2.22 HRTEM image of $Al_{90}Sm_5Tb_5$ indicating fcc-Al nanocrystal

2.4.3.2   Atom Probe Tomography Results

Both $Al_{90}Y_5Tb_5$ and $Al_{90}Sm_5Tb_5$ alloy systems were analyzed with APT. As it is previously stated in section 2.3.4, during sample preparation of APT experiments, ribbons of both compositions are heated up until the onset temperature of their first crystallization reaction in their own DSC traces and then rapidly cooled down to room temperature. Therefore, the first reactions were interrupted for both samples. In this section, the Ga atoms coming from the FIB Ga^+ etching process are ignored, and only Al, Y, Sm, and Tb atoms are considered for the analyses.

The APT results of $Al_{90}Y_5Tb_5$ are shown in the below figures. In Figure 2.23, the atom distributions throughout the sample are revealed. Only 10% of Al atoms, 50% of Y, and 50% of Tb atoms are displayed in this figure. It is observed that Al atoms are distributed homogeneously whereas, this is not the case for Y and Tb atoms. From the in-situ HEXRD analyses and TEM micrographs, it is known that during devitrification of amorphous $Al_{90}Y_5Tb_5$ ribbons, in the first reaction, Al nanocrystals are formed in the amorphous matrix. APT results also support this outcome. In Figure 2.23, some Y and Tb depleted regions exist, which shows that there are nearly pure Al regions as a sign of emerging Al nanocrystals.

Figure 2.23 Atom distributions of (a) all atoms, (b) Al atoms (10%), (c) Y atoms (50%) and (d) Tb atoms (50%)

Isosurfaces shown in Figure 2.25 are created based on Al atomic concentrations. There are almost pure Al regions of 20-30 nm in length. The core of the isosurfaces is purer compared to the outer regions. From the EDS results tabulated in section 2.4.1, it is known that the composition of the as-spun sample is almost $Al_{90}Y_5Tb_5$, and the elements are distributed homogeneously throughout the sample. However, during the first reaction, Al atoms accumulate together, forming the fcc-Al nanocrystals, and the rare-earth elements are diffused away from the nanocrystals. In Figure 2.24, the 1D concentration profile between two Al nanocrystal regions is shown. The region between the nanocrystals shows approximately 80% Al atom distribution, whereas there exists almost 20% Y and Tb atoms in total.
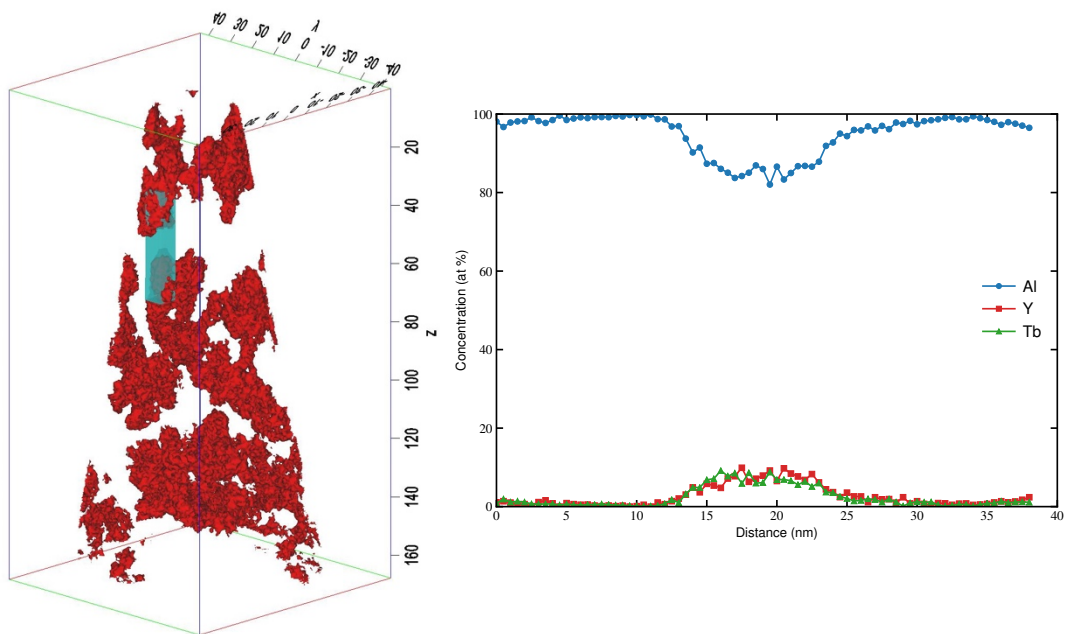
Figure 2.24 1D concentration profile of the selected ROI in 95% Al isosurface of $Al_{90}Y_5Tb_5$ system
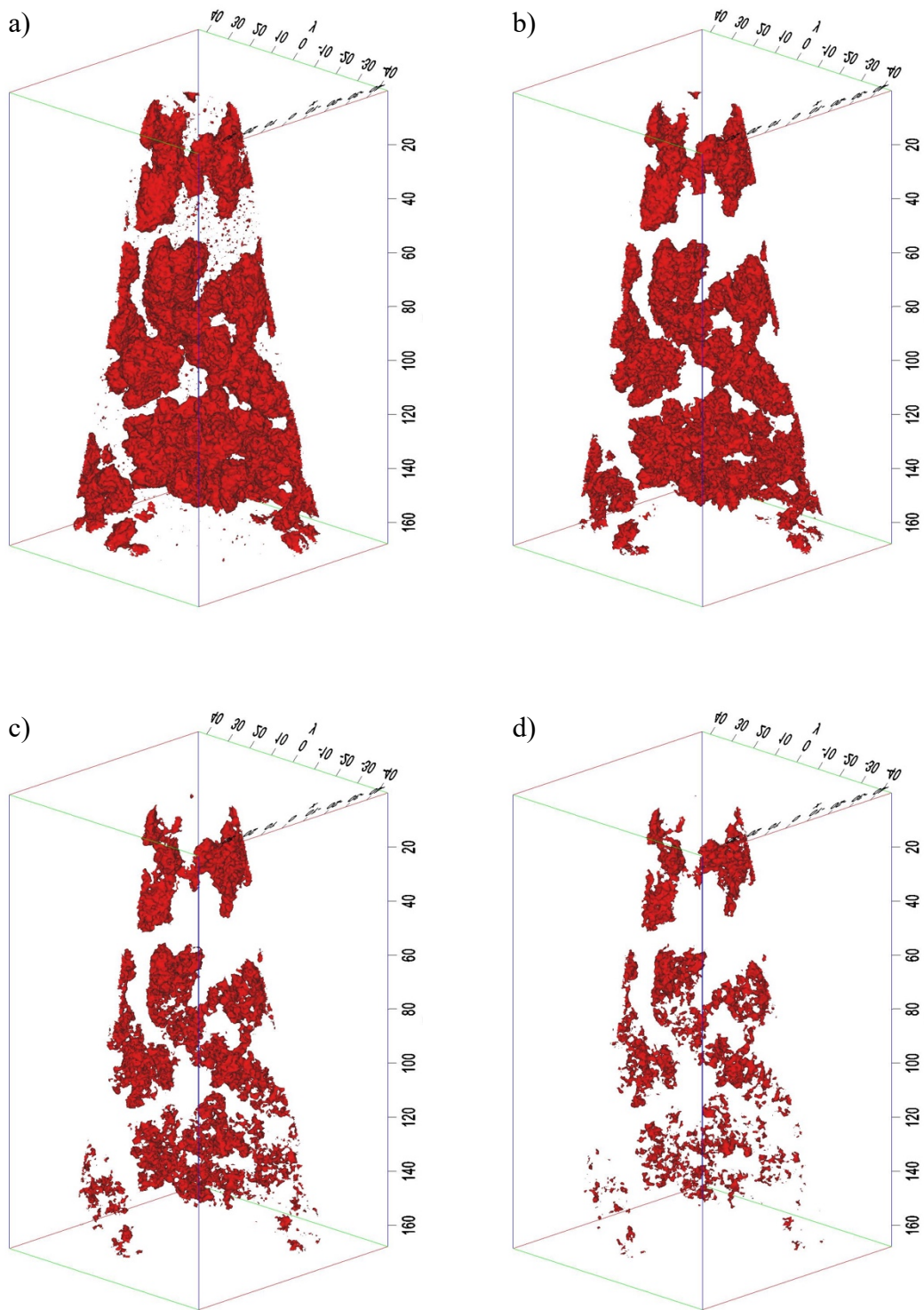
Figure 2.25 Isosurfaces of (a) 90%, (b) 95%, (c) 98% and (d) 99% Al atomic concentrations in $Al_{90}Y_5Tb_5$ sample

Shapes and sizes of $Al_{90}Y_5Tb_5$ and $Al_{90}Sm_5Tb_5$ sample tips differ due to the processing and Ga^+ sharpening during FIB sample preparation. The atom distributions throughout the $Al_{90}Sm_5Tb_5$ sample are displayed in Figure 2.26. Only 10% of Al atoms, 50% of Sm, and 50% of Tb atoms are displayed in this figure. Similar to the $Al_{90}Y_5Tb_5$ system, there are Al-rich, or in other words, rare-earth element depleted regions in the sample. The isosurfaces displayed in Figure 2.27 are created based on Al atomic concentrations. Almost pure Al regions exist, and the average sizes are similar to Al nanocrystals in the $Al_{90}Y_5Tb_5$ structure. However, unlike the $Al_{90}Y_5Tb_5$ system, almost pure Al regions' shape and size distribution are wide.

1D concentration profile between two randomly selected Al nanocrystals is presented in Figure 2.28. It is observed that the average concentration of the region between nanocrystals is 90% Al and 10% Sm and Tb in total. In addition, Al amount never falls below 88% in any region. Generally, in Al-RE marginal glass-forming systems, a very high density of Al nuclei arises during the first crystallization event, and the concentration of the remaining amorphous matrix becomes rare-earth element rich. However, this is not the case for this unique $Al_{90}Sm_5Tb_5$ alloy system. The 1D concentration profile implies that the diffusion is restricted for this system, and crystallization occurs with no or little composition change of the amorphous phase. Since the peak shape and broadness in DSC determines the kinetics and rate of a reaction, the sharpness of first the crystallization peak in the $Al_{90}Sm_5Tb_5$ system also supports this outcome. As the diffusion is limited, the reaction takes place very rapidly.
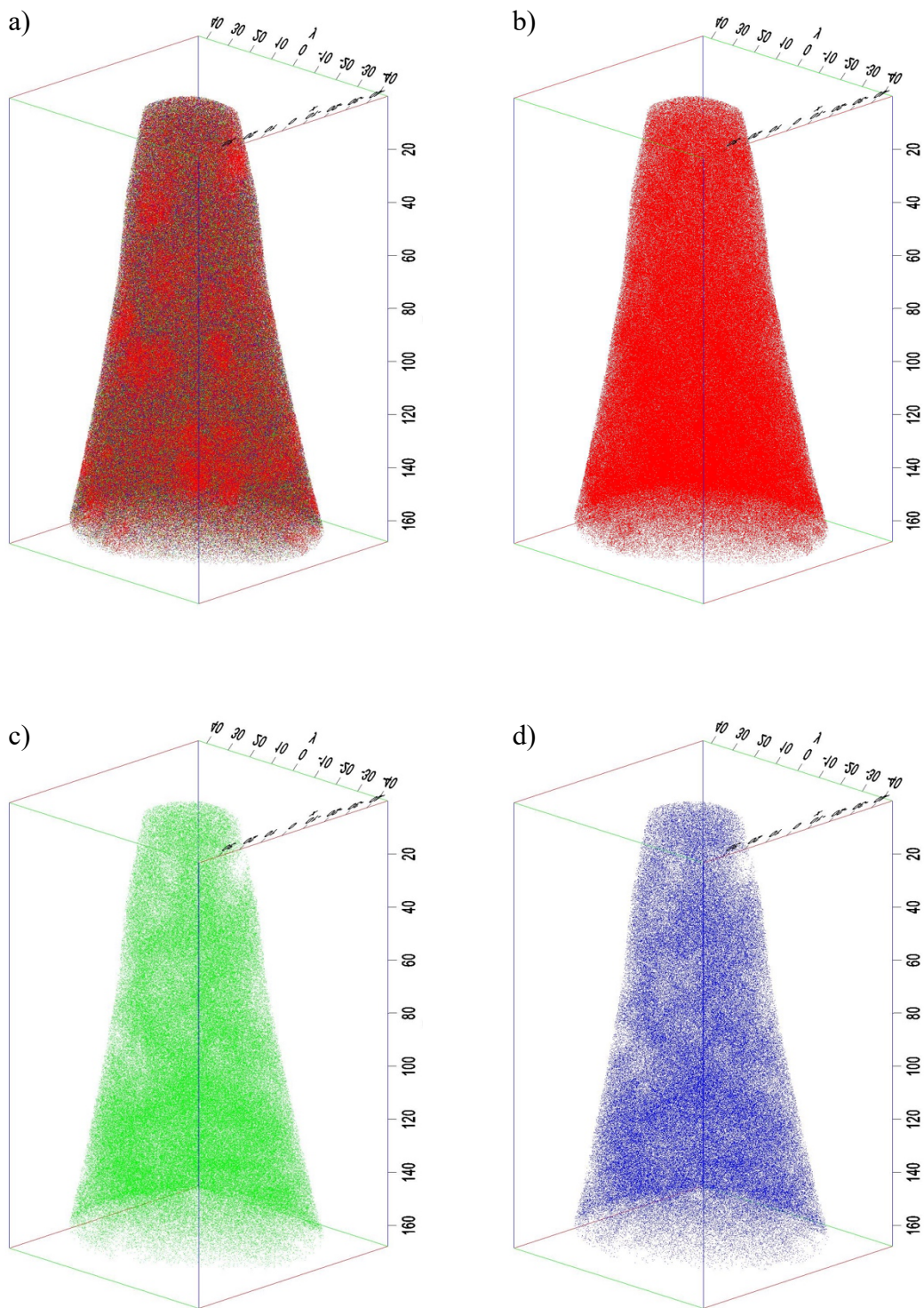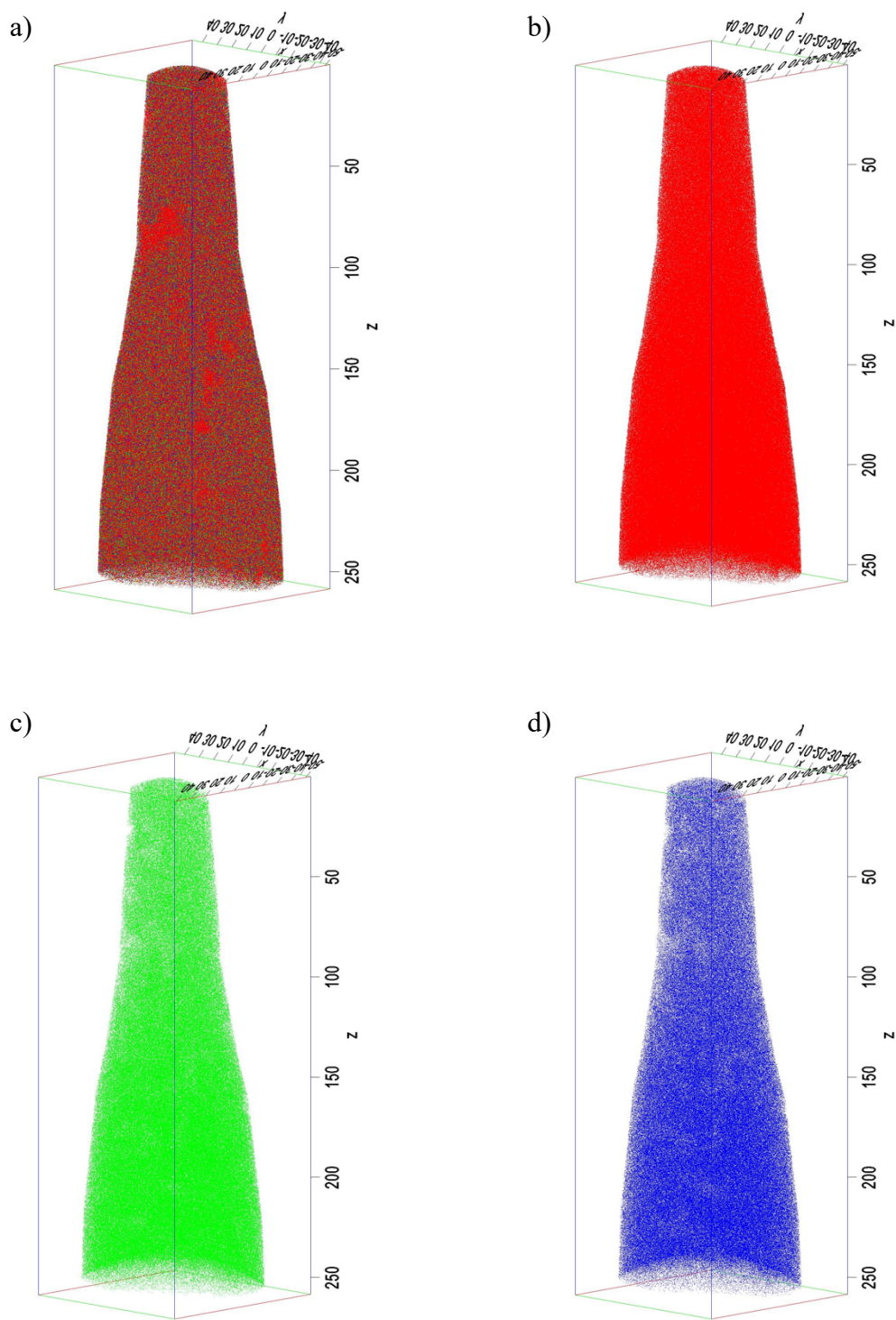
Figure 2.26 Atom distributions of (a) all atoms, (b) Al atoms (10%), (c) Sm atoms (50%) and (d) Tb atoms (50%)
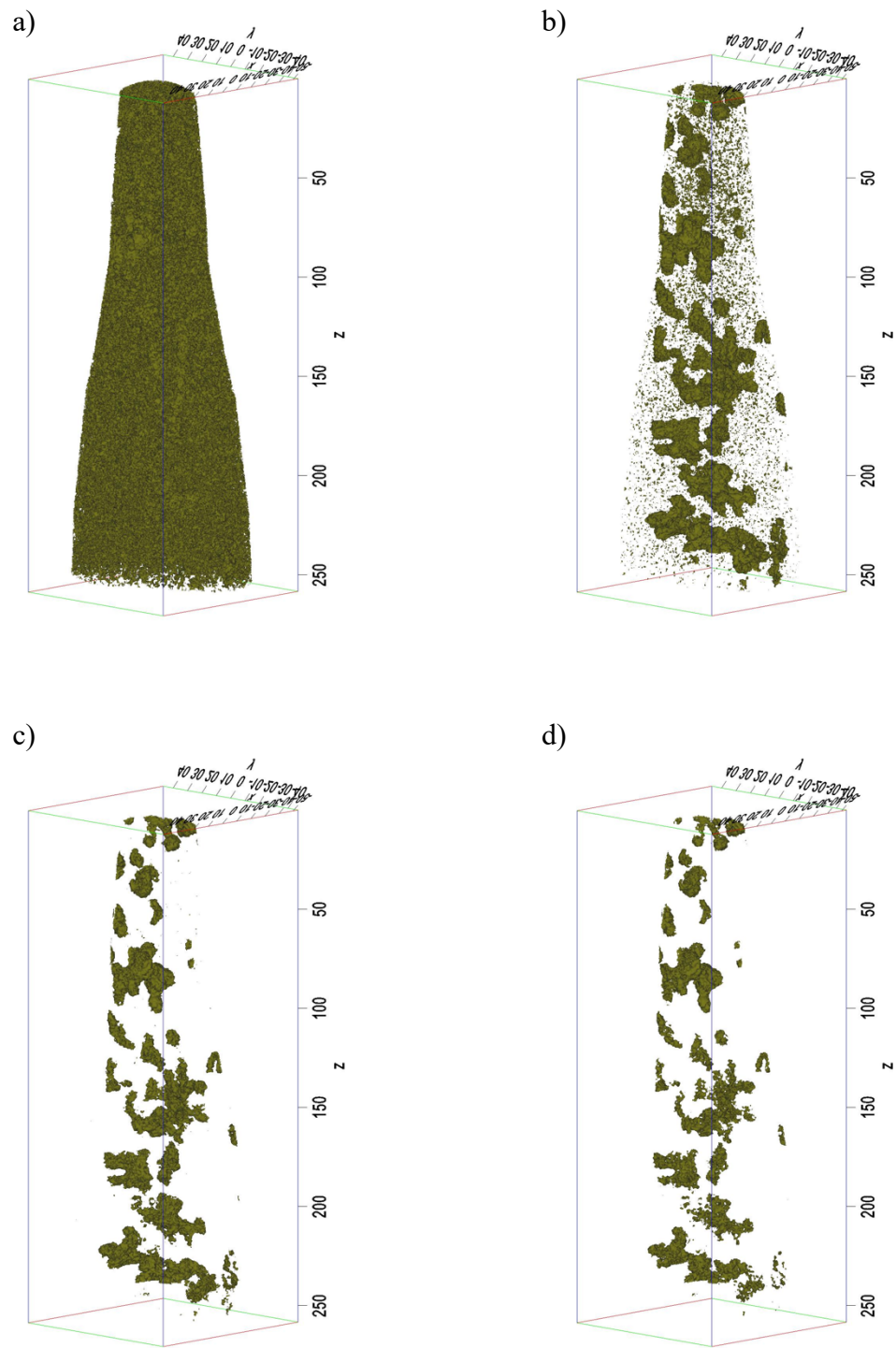
Figure 2.27 Isosurfaces of (a) 90%, (b) 95%, (c) 98% and (d) 99% Al atomic concentrations in $Al_{90}Sm_5Tb_5$ sample
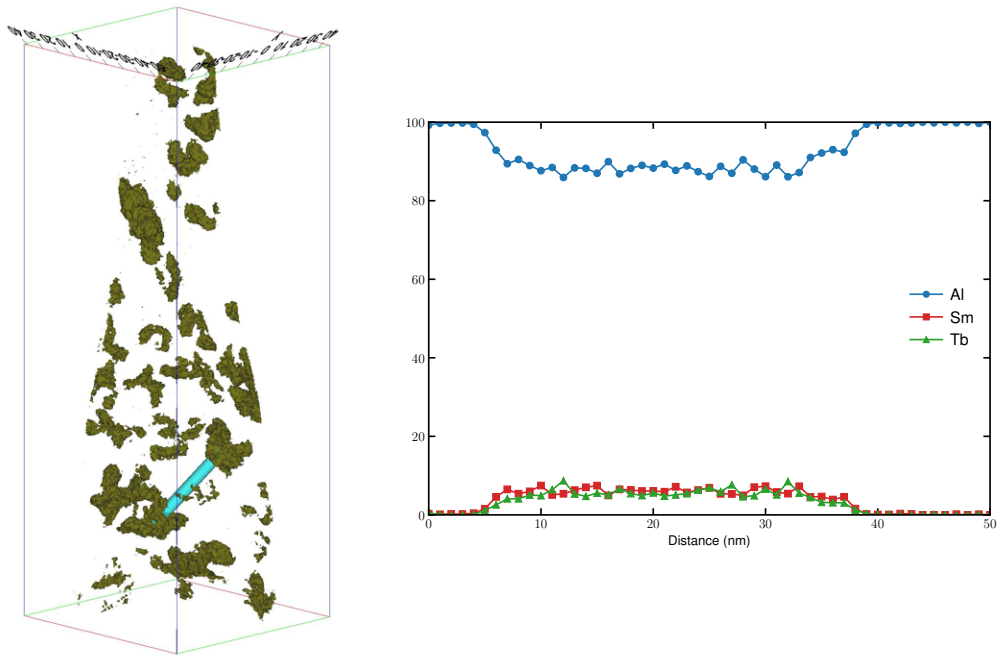
Figure 2.28 1D concentration profile of the selected ROI in 95% Al isosurface of $Al_{90}Sm_5Tb_5$ system

For the $Al_{90}Y_5Tb_5$ and $Al_{90}Sm_5Tb_5$ samples, randomly, ten nanocrystals are selected in the TEM images as given in Figure 2.29, and their largest dimensions in 2D are measured. The average of random measurements resulted as 23 nm for $Al_{90}Y_5Tb_5$ sam 27.5 nm for $Al_{90}Sm_5Tb_5$ sample. Supporting, in Figures 2.24 and 2.28, nanocrystals of 20-30 nm in length were detected by APT.
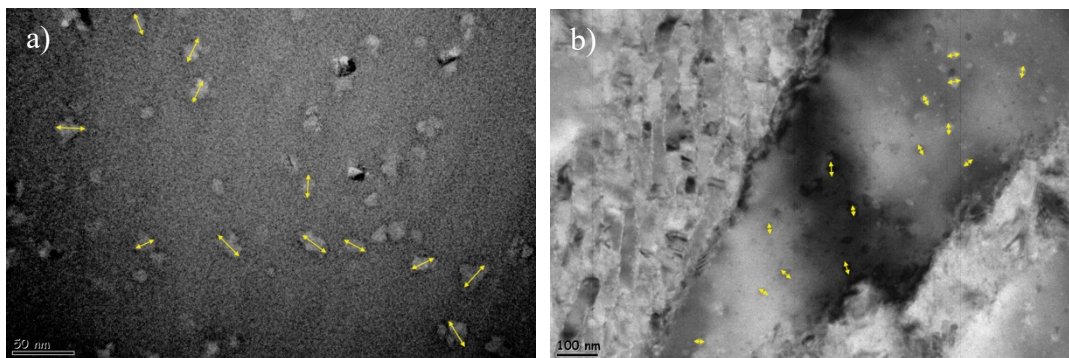
Figure 2.29 TEM images for nanocrystal size measurement after the interrupted first crystallization event of (a) $Al_{90}Y_5Tb_5$ and (b) $Al_{90}Sm_5Tb_5$ sample

50

2.5 Conclusion

The effects of short-range chemical order in ternary marginal glass-forming systems of $Al_{90}Sm_5Tb_5$ and $Al_{90}Y_5Tb_5$ on crystallization pathway upon heating is investigated in detail with a comprehensive study of DSC, HEXRD, TEM, and APT. $Al_{90}Y_5Tb_5$ glassy system showed a similar crystallization behavior to $Al_{90}RE_{10}$ binary metallic glass systems. At first, fcc-Al nanocrystals are formed on the amorphous matrix upon devitrification. The sizes of nanocrystals are determined to be 20-25nm in their largest dimension by APT and TEM. Then with a second exothermic reaction, the intermetallics form in the structure.

On the other hand, the $Al_{90}Sm_5Tb_5$ composition shows different behavior. There is no exothermic reaction that solely belongs to fcc-Al formation. Upon heating, fcc-Al nanocrystals arise with one or more intermetallic phases at the same time. TEM analyses showed that Al nanocrystals are dispersed in a crystal matrix with 20-25 nm in their largest dimension, supported by APT results, similar to $Al_{90}Y_5Tb_5$. 1D concentration profiles of APT studies showed that the nanocrystals are almost pure Al, whereas the Al concentration falls to 80 at% in the region between the nanocrystals. On the other hand, the Al concentration never drops below 88% for the $Al_{90}Sm_5Tb_5$ sample. The results showed that in addition to their physical contributions, the RE elements also have chemical effects on the kinetics of the glassy system. When 5% of Tb is replaced by 5% Sm, the devitrification pathway is altered.

CHAPTER 3

INITIAL CRYSTALLIZATION KINETICS OF Al$_{90}$Sm$_5$Tb$_5$ MARGINAL GLASS FORMING ALLOY

3.1 Introduction

Thermal analyses, such as DSC, TGA, or DTA, play a crucial role in understanding the kinetics of a reaction. Conducting DSC experiments can lead to many critical thermal parameters, including glass transition temperature (T_g), crystallization onset temperature (T_x), crystallization peak temperature (T_p), melting temperature ($T_{m,}$) enthalpy of a reaction (ΔH), or heat. In addition to this straightforwardly obtained information, further kinetic analyses can be made from DSC data to find out more detailed information such as nucleation and growth mechanisms of a system or activation energy (E_a). In this chapter, the kinetics of the first crystallization reaction of the Al$_{90}$Sm$_5$Tb$_5$ ternary glass-forming system is investigated in detail by DSC experiments.

3.2 Literature Review

3.2.1 Differential Scanning Calorimetry (DSC)

Differential Scanning Calorimetry (DSC) is a simple yet powerful characterization tool to determine physical and thermal properties of materials such as activation energy (E_a), crystallization temperature (T_x), glass transition (T_g), change in enthalpy (ΔH), or melting point (T_m) precisely by changing heat flow or changing temperature. It has been used widely due to advantages like low cost, fast and reliable results, a low amount of sample, availability for liquid and solid materials.

A DSC equipment can be used to conduct experiments in two different modes as isothermal or non-isothermal. For the isothermal analysis, the sample is rapidly heated up to the desired temperature and held at that temperature as long as required. After the completion of the experiment, the sample is cooled down to room temperature. For non-isothermal, or in other words, isochronal experiments, the sample is heated with a constant heating rate and then cooled down to room temperature. This type of experiment does not include a dwell time at any temperature.

DSC can notice many thermal activities in material showing whether they are endothermic or exothermic. When an amorphous metallic sample is investigated under a constant heating rate, the sample first shows an endothermic relaxation and glass transition behavior. Then crystallization takes place in a single or multiple-step(s). Finally, the alloy melts at T_m if the temperature range of DSC is convenient. The first and second-order reactions can be detected and discussed by evaluating DSC outputs. In Figure 3.1, a schematic DSC curve showing heat flow against temperature is displayed.
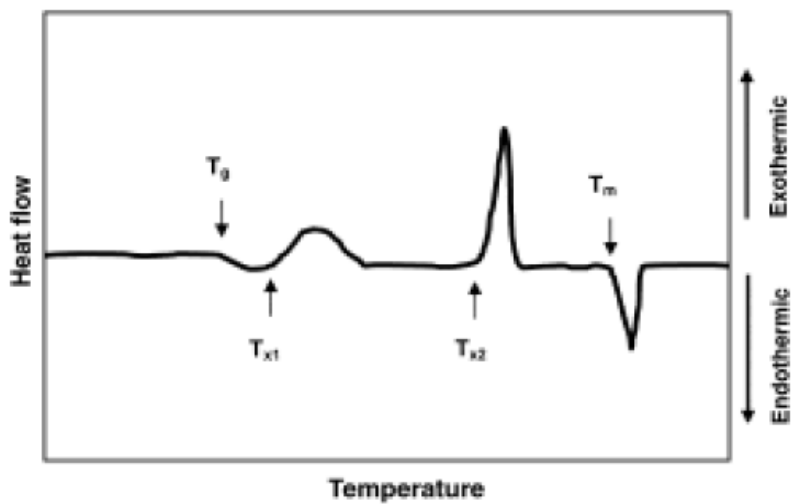
Figure 3.1 Representative DSC curve with indicated important kinetic parameters (Adopted from [54])

3.2.2   Kissinger and Ozawa Analysis Method

Kissinger analysis is one of the most common methods to explain the kinetic model by estimating the activation energies of crystallization reactions in a glass-forming system. When the heating rate is kept constant, DSC detects exothermic peaks of crystallization. Activation energy calculation can be made at any temperature of the selected reaction. However, Kissinger assumes that at T_p, the reaction rate is at its higher degree. Therefore, making calculations and estimations at T_p of a reaction is more meaningful.

$$\ln\left(\frac{T^2}{\Phi}\right) = \frac{E_c}{RT} + \ln\left(\frac{E_c}{k_0 R}\right) \qquad\qquad Eq.\,3.1$$

A simplified Kissinger formula used for the determination of activation energy is given in Eq. 3.1 where Φ is the constant heating rate, E_c is the activation energy, R is the ideal gas constant, T is the selected temperature, and k_0 is a material constant. When Kissinger plot of $\ln(\Phi/T^2)$ against 1/T is drawn with three or more constant heating rate experimental data, the effective activation energy can be calculated from the slope [55], [56].

Ozawa analysis is another extensive method for investigating kinetic behavior. According to the Ozawa method, Eq 3.2 implies the activation energy calculation where Φ is the constant heating rate, E_c is the activation energy, R is the ideal gas constant, T is the temperature, and C is a constant [57], [58].

$$\ln(\Phi) = -1.0516\frac{E_c}{RT} + C \qquad\qquad Eq.\,3.2$$

When Φ against 1/T graph is prepared with three or more different heating rate experimental data, E_c can be found from the slope of a linear fit to the data points, similar to Kissinger method.

3.2.3 Non-Isothermal JMAK Calculations

Solid-state transformations can be described by JMAK (Johnson-Mehl-Avrami-Kolmogorov) equations. Unlike earlier classical kinetic theory, the JMAK approach involves nucleation and growth mechanisms. This theory accepts random nucleation and isotropic growth estimates fraction transformed in a solid-state to time. A simplified JMAK equation for isothermal transformations is given in Eq. 3.3 where x is the transformed or recrystallized fraction at time t, K is the kinetic rate constant, and n is the Avrami exponent [59].

$$x(t) = 1 - \exp(-Kt^n) \qquad\qquad Eq.\,3.3$$

Henderson showed that the JMAK equation could also be adapted to non-isothermal transformations. Since the isothermal transformation rate d(x)/d(t) is directly proportional to dH/dt, the transformed fraction (x) can be calculated by using Eq. 3.4 where H_∞ is the total enthalpy change of the transformation reaction and H(T) is the enthalpy change up to temperature T [60].

$$x = \frac{\int_{T_0}^{T} \left(\frac{dH_c}{dT}\right) dT}{\int_{T_0}^{T_\infty} \left(\frac{dH_c}{dT}\right) dT} = \frac{H(T)}{H_\infty} \qquad\qquad Eq.\,3.4$$

When the transformed fraction (x) at any temperature (T) is calculated, the non-isothermal Avrami exponent (n) can be calculated using Eq. 3.5 where x is the transformed fraction, T is the temperature, E_a is the Kissinger activation energy, and R is the gas constant.

$$\frac{\ln[-\ln(1-x)]}{1/T} = -\frac{nE_a}{R} \qquad\qquad Eq.\,3.5$$

3.2.4 Local Activation Energy Calculations

Even though E_c stands for average activation energy, also called effective activation energy, and this parameter is used in Kissenger and Ozawa's approaches, the mechanism of nucleation and growth and details of the process cannot be fully understood unless local activation energy is taken into consideration. Crystallization is controlled by nucleation and growth, and activation energy is not constant throughout the process. It is known that activation energy stands for a critical role in understanding the thermal behavior of a material. The structure that has higher activation energy is more stable than the one that has lower activation energy. Therefore, to understand and explain the non-isothermal process in detail, local activation energy should be inserted into Kissinger and Ozawa's analysis. The Kissinger and Ozawa equations adapted for local activation energy calculations are given in Eq. 3.6 and Eq. 3.7, respectively.

$$\ln\left(\frac{T(x)^2}{\Phi}\right) = \frac{E_c(x)}{RT(x)} + \ln\left(\frac{E_c(x)}{k_0 R}\right) \qquad Eq.\,3.6$$

$$\ln(\Phi) = -1.0516\frac{E_c(x)}{RT(x)} + C \qquad Eq.\,3.7$$

3.3 Experimental Procedure

Melt-spun ribbons of $Al_{90}Sm_5Tb_5$ amorphous alloys are produced in Ames Laboratory, USA. For the experiments of thermal analyses, Q2000 DSC equipment of TA instruments brand is used. The procedural details of sample production and DSC experiments are similar to the ones described in Chapter 2. Distinctly, in this chapter, the DSC experiments are held between 300-575 K with heating rates of 10 K/min, 20 K/min, 30 K/min, and 40 K/min, respectively.

3.4   Results and Discussion

Isochronal DSC heating curves of $Al_{90}Sm_5Tb_5$ melt-spun ribbons at different heating rates of 10 K/min, 20 K/min, 30 K/min, and 40 K/min are given in Figure 3.2. From the characterization studies present in Chapter 2, it is known that as-spun ribbons have an amorphous structure. The amorphous alloy undergoes two exothermic reactions upon heating, whereas there is no distinct endothermic reaction indicating glass transition before crystallization. In DSC analyses, the sharper peak is mainly related to faster transformation [61]. Therefore, as the heating rate increases from 10 K/min to 40 K/min, the exothermic peaks become sharper with a more definite enthalpy change. As the heating rate increases, Tx and Tp values shift to higher temperatures, showing that the crystallization reactions are heating rate dependent and, therefore, time-dependent.
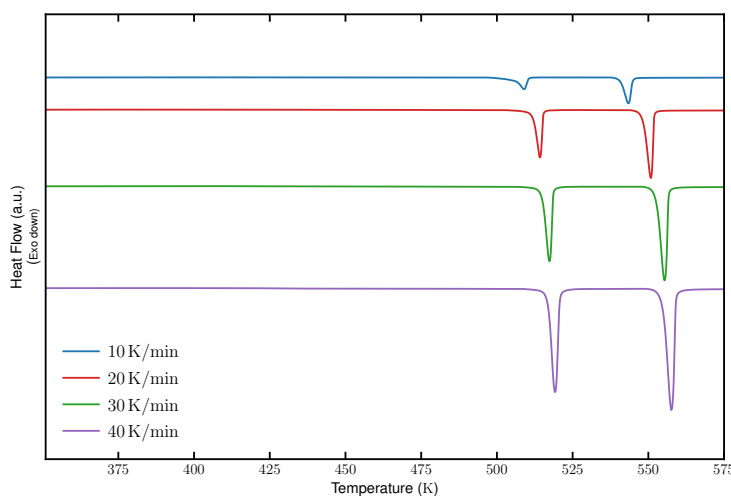
Figure 3.2 Isochronal DSC heating curves of melt-spun $Al_{90}Sm_5Tb_5$ marginal glass former alloy at 10K/min, 20 K/min, 30K/min, and 40 K/min heating rates

The isochronal DSC data is tabulated for each heating rate in Table 3.1, and the corresponding Kissinger and Ozawa plots are shown in Figure 3.3. The Kissinger method and the Ozawa method calculations are done according to Eq. 3.1and Eq. 3.2, respectively. Since the DSC experiments are carried out at four different heating

rates, four data points are acquired for each method. The corresponding average activation energies (E_c) are determined from the slopes of the linear best fits to those four data points and are listed in Table 3.2. The E_c values calculated by different methods show slight deviations, which can be accepted within the error limits. The activation energy calculated at T_x shows the required energy of transformation from the supercooled liquid state to the crystallization state. T_p is related to crystal growth, and it is considered the point where the reaction rate is highest [62].

Table 3.1 Isochronal DSC data of $Al_{90}Sm_5Tb_5$ melt-spun alloy

ϕ (K/min)	1st peak Tx (K)	1st peak Tp (K)	2nd peak Tp (K)
10	506	509	543
20	512	514	551
30	515	517	555
40	517	519	558
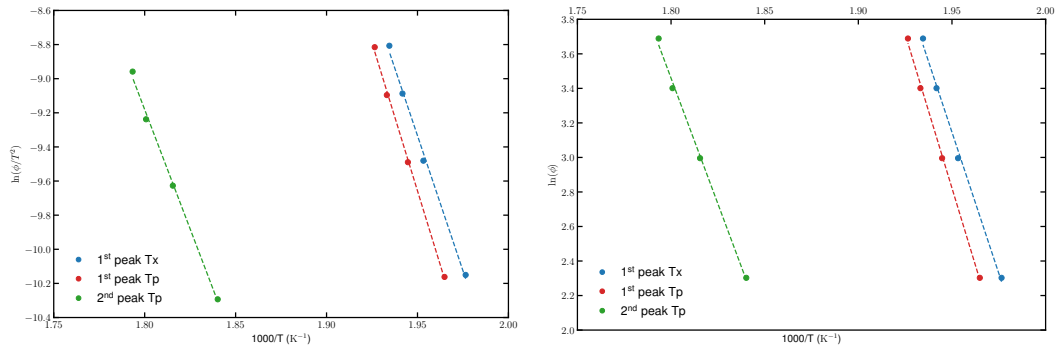
Figure 3.3 (a) Kissinger and (b) Ozawa plots of melt-spun $Al_{90}Sm_5Tb_5$ ternary alloys

According to the calculations, the second exothermic reaction requires less energy at T_p (233 kJ/mol according to Kissinger method and 230 kJ/mol according to Ozawa method) than the first exothermic reaction at T_p (289 kJ/mol according to Kissinger method and 282 kJ/mol according to Ozawa method). However, it must be

considered that the first reaction is a crystallization reaction realizing from a fully amorphous structure. On the other hand, the second reaction starts from an already crystallized structure.

Table 3.2 Activation energies of first and second exothermic reactions calculated according to Kissinger and Ozawa methods

Crystallization Reaction	Kissinger E_c (kJ/mol)	$|r|$	Ozawa E_c (kJ/mol)	$|r|$
1st peak Tx	263	0.9980	258	0.9980
1st peak Tp	289	0.9992	282	0.9992
2nd peak Tp	233	0.9985	230	0.9886

In Table 3.3, the average activation energies of $Al_{90}Sm_5Tb_5$ at T_p of the first reaction are given compared to $Al_{90}Sm_{10}$ and $Al_{90}Tb_{10}$. All samples were melt-spun ribbons with initially amorphous structures. It is observed that the required activation energy of ternary alloy is in between the required activation energies of binary alloys reported by Yıldırım [63] and Kalay [43].

Table 3.3 Activation energies of first reactions of binary and ternary marginal glass former alloys calculated according to Kissinger and Ozawa methods

Composition	Kissinger E_c (kJ/mol)	Ozawa E_c (kJ/mol)	Ref
$Al_{90}Sm_5Tb_5$	289 ± 9	282 ± 9	This work
$Al_{90}Sm_{10}$	171 ± 3	171 ± 2	[43]
$Al_{90}Tb_{10}$	298 ± 1	291 ± 1	[63]
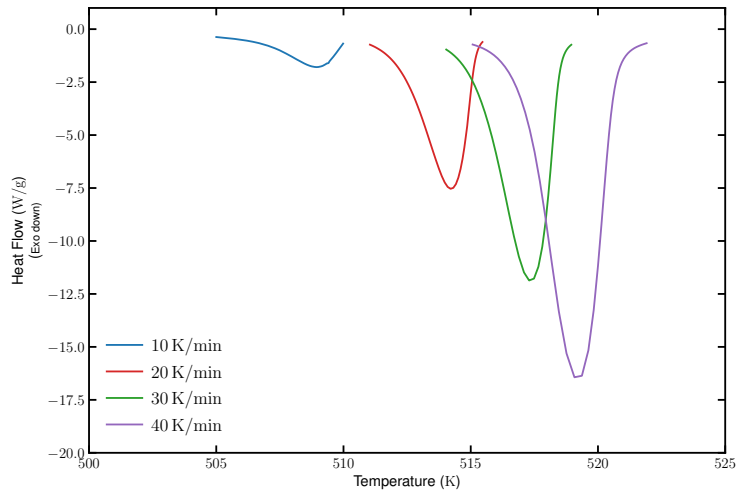
Figure 3.4 Isochronal DSC curves of only first transformation reactions at 10K/min, 20K/min, 30K/min, and 40K/min heating rates of $Al_{90}Sm_5Tb_5$ partially crystallized alloy

Figure 3.4 demonstrates only the first exothermic peaks of 10 K/min, 20 K/min, 30 K/min, and 40 K/min heating rates, respectively. Peak shapes of 20 K/min, 30 K/min, and 40 K/min heating rates data are similar and symmetrical. In contrast, the data belonging to the 10 K/min heating rate is asymmetrical and different. The kinetics of a reaction determines the peak shape itself, and it is directly related to the Avrami coefficient, n [53], [56]. A study conducted by Kissinger [56] revealed that as n decreases, the amount of undecomposed reactant at T_p also decreases and the shape of the exothermic peak becomes asymmetrical. Therefore, the data of 10 K/min heating rate is not included in the analyses thereafter.
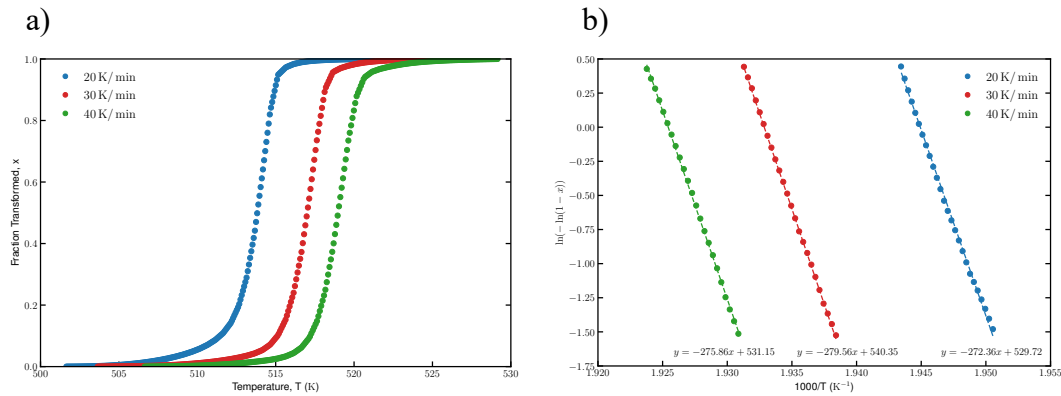
Figure 3.5 a) Transformed fraction and b) Non-isothermal Avrami plots of $Al_{90}Sm_5Tb_5$ calculated by 10 K/min, 20 K/min, and 30 K/min heating rate data

Figure 3.5(a) shows the sigmoidal curves of transformed fraction in the first exothermic event upon crystallization with respect to temperature for 20 K/min, 30 K/min, and 40 K/min heating rates. The fraction transformed (x) at a specific temperature T can be calculated by Eq. 3.4, where T_0 is the onset temperature, T_∞ is the ending temperature of the kinetic event, and dH_c/dT is the heat capacity [53]. Therefore, H(T) can be estimated by the area under the DSC curve to the desired temperature, T, where H_∞ is the total area between T_0 and T_∞ temperatures.

Plots of ln(-ln(1-x)) against 1000/T and the linear best-fit equations are presented in Figure 3.5(b) for 20 K/min, 30 K/min, and 40 K/min heating rates. The plots are valid only for transformation range where $0.2 < x < 0.8$. The non-isothermal Avrami coefficients (n) calculated from the slopes according to Eq. 3.5 are found as 7.84, 8.04, and 7.94 for 20 K/min, 30 K/min, and 40 K/min heating rates. Kissinger activation energy, which is 289 kJ/mol, is used for the calculations instead of Ozawa activation energy.
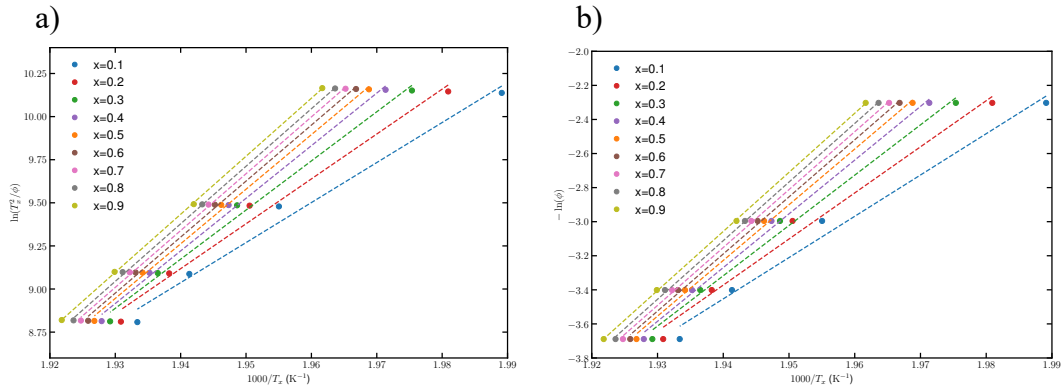
Figure 3.6 Plots for calculating local activation energies under non-isothermal heating according to (a) KAS and (b) OFW methods for $Al_{90}Sm_5Tb_5$ ternary alloy

Kissinger and Ozawa activation energies give information about the overall reaction kinetics. However, most of the time, it is also crucial to evaluate the local activation energies. The characteristic sigmoidal volume fraction curves indicate that the crystallization rate gradually increases up to x=0.2. Between 0.2 < x < 0.8, it shows a linear and drastic step-up, and after x=0.8, reaction rate slows down. Since the reaction kinetics are not constant throughout the event, the change in activation energies also supplies valuable information. The KAS and OFW plots between 0.1 < x < 0.9 transformation range and corresponding local KAS and OFW activation energies versus transformed fraction plots are shown in Figure 3.6 and Figure 3.7.
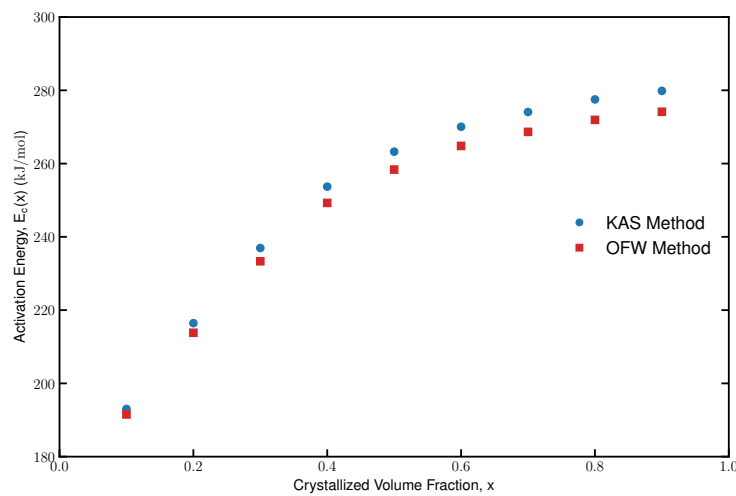
Figure 3.7 Local activation energy plots according to KAS and OFW methods

3.5   Conclusion

In this chapter, initial crystallization kinetics of $Al_{90}Sm_5Tb_5$ ternary glassy alloy upon devitrification are investigated by DSC experiments. The analyses were based on non-isothermal (isochronal) heating experiments. It is found out that there is no definite glass transition signal in DSC curves. The exothermic crystallization peaks shift to higher temperature values with sharper peaks and more enthalpy change requirements as the heating rate increases. The effective and local activation energies are calculated according to both Kissinger and Ozawa methods. Surprisingly, the local activation energy tends to increase from the beginning to the end of the first crystallization reaction, contrasting with the fcc-Al nanocrystal formation reaction.

CHAPTER 4

CONCLUSIONS AND FUTURE RECOMMENDATIONS

4.1 Conclusions

In this thesis study, the effects of rare-earth elements on the devitrification pathway of ternary marginal glass formers are investigated. Metallic glasses of $Al_{90}Sm_5Tb_5$ and $Al_{90}Y_5Tb_5$ compositions are produced by melt-spinning, and their crystallization behavior is studied by experimental DSC, HEXRD, TEM, and APT tools.

In the first part of this study, the amorphous as-spun structures of samples are confirmed by room temperature HEXRD and bright-field TEM analyses. Then the amorphous ribbons are subjected to controlled crystallization experiments with a 10 K/min heating rate. Initial results showed that the $Al_{90}Y_5Tb_5$ composition forms a high density of fcc-Al nanocrystals in the amorphous matrix upon heating, and then the intermetallics arise. This behavior is similar to previously studied crystallization pathways of $Al_{90}Tb_{10}$ and $Al_{90}Sm_{10}$ binary systems [41], [44], [64], [65]. However, $Al_{90}Sm_5Tb_5$ did not show a different fcc-Al nanocrystal formation reaction. Fcc-Al nanocrystals and one or more intermetallic phases are originated from the amorphous structure at the same time. The APT and TEM analyses confirmed that fcc-Al nanocrystals of 20-25 nm in length are formed in the first crystallization event for $Al_{90}Sm_5Tb_5$ and $Al_{90}Y_5Tb_5$ compositions.

In the second part, the initial crystallization of $Al_{90}Sm_5Tb_5$ glassy alloy is further investigated by DSC in terms of the kinetics of the reaction. Non-isothermal heating experiments are conducted with four different heating rates. It is observed that as the heating rate increases, the exothermic events of crystallization are shifted to higher temperature values with sharper peaks and more definite enthalpy change. The local

activation energy calculations based on KAS and OFW methods showed that the required energy tends to increase from the beginning of the reaction to the end.

4.2   Future Recommendations

The motivation of this thesis work was to understand whether the RE elements have a chemical influence on the structure of Al-based marginal glass formers or they only contribute with their physical properties. The studies resulted that although the RE content is kept constant at 10 at%, the replacement of 5% Tb with 5% Sm altered the crystallization pathway. However, the mechanisms and kinetics behind this behavior still need to be enlightened. Previous studies on the $Al_{90}Tb_{10}$ system showed that melt-spun ribbons and magnetron sputtered thin films of the same composition resulted in different crystallization behavior [44], [46], [47]. The reason is thought to be the differences in amorphous structures. The initial structure is liquid for the melt-spinning process, where the cooling rate is 10^5-10^6 K/s. On the other hand, magnetron sputtered thin films are originated from the vapor phase with a 10^{12} K/s cooling rate.

The differences between the crystallization kinetics of $Al_{90}Sm_5Tb_5$ and $Al_{90}Y_5Tb_5$ are also thought to be related to their amorphous structures. For further investigations on the chemical contribution of RE elements, the amorphous structures and the liquid structures of molten states should be analyzed in detail. The first crystallization event of $Al_{90}Sm_5Tb_5$ is completed very fast, and the initial amorphous phase was completely decomposed before T_p of the kinetic event. Hence, there might be some MRO clusters that ease the nucleation upon heating. In addition, it is observed that diffusion is very limited for this composition. Although almost pure Al nanocrystals are formed, the Al content of the regions between the Al regions did not fall below 88 at%. These results imply that the crystallization is completed with restricted diffusion.

With conventional experimental tools and characterization methods, it is very hard to investigate the characteristics of the liquid state. Therefore, modeling and simulation should also be considered as future studies for the investigation of $Al_{90}Sm_5Tb_5$. It is essential to support the experimental outcomes with modeling and simulation. Therefore, RMC or MD techniques can be used.

REFERENCES

[1]   M. F. Ashby and A. L. Greer, "Metallic glasses as structural materials," *Scr. Mater.*, vol. 54, no. 3, pp. 321–326, 2006, doi: 10.1016/j.scriptamat.2005.09.051.

[2]   W. Klement, R. H. Willens, and P. Duwez, "Non-crystalline structure in solidified gold-silicon alloys," *Nature*, vol. 187, p. 869, 1960.

[3]   P. Duwez, "Metallic glasses-historical background," pp. 19–23, 1981, doi: 10.1007/3540104402_2.

[4]   M. H. Cohen and D. Turnbull, "Composition requirements for glass formation in metallic and ionic systems," *Nature*, vol. 189, pp. 131–132, 1961.

[5]   H. . Chen and D. Turnbull, "Formation, stability and structure of palladium-silicon based alloy glasses," *Acta Metall.*, vol. 17, no. 8, pp. 1021–1031, 1969.

[6]   H. S. Chen and D. Turnbull, "Evidence of a glass-liquid transition in a gold-germanium-silicon alloy," *J. Chem. Phys.*, vol. 48, no. 6, pp. 2560–2571, 1968, doi: 10.1063/1.1669483.

[7]   M. C. Lee, J. M. Kendall, and W. L. Johnson, "Spheres of the metallic glass Au55Pb22.5Sb 22.5 and their surface characteristics," *Appl. Phys. Lett.*, vol. 40, no. 5, pp. 382–384, 1982, doi: 10.1063/1.93110.

[8]   H. W. Kui, A. L. Greer, and D. Turnbull, "Formation of bulk metallic glass by fluxing," *Appl. Phys. Lett.*, vol. 45, no. 6, pp. 615–616, 1984, doi: 10.1063/1.95330.

[9] A. Inoue, T. Nakamura, T. Sugita, T. Zhang, and T. Masumoto, "Bulky La-Al-TM (TM = transition metal) amorphous alloys with high tensile strength produced by a high-pressure die casting method," *Mater. Trans. JIM*, vol. 34, no. 4, pp. 351–358, 1993, doi: 10.2320/matertrans1989.34.351.

[10] A. Inoue, A. Kato, T. Zhang, S. G. Kim, and T. Masumoto, "Mg-Cu-Y amorphous alloys with high mechanical strengths produced by a metallic mold casting method," *Mater. Trans. JIM*, vol. 32, pp. 609–616, 1991.

[11] A. J. Drehman, A. L. Greer, and D. Turnbull, "Bulk formation of a metallic glass: Pd40Ni40P 20," *Appl. Phys. Lett.*, vol. 41, no. 8, pp. 716–717, 1982, doi: 10.1063/1.93645.

[12] Y. Q. Cheng and E. Ma, "Atomic-level structure and structure-property relationship in metallic glasses," *Prog. Mater. Sci.*, vol. 56, no. 4, pp. 379–473, 2011, doi: 10.1016/j.pmatsci.2010.12.002.

[13] M. Chen, "A brief overview of bulk metallic glasses," *NPG Asia Mater.*, vol. 3, no. 9, pp. 82–90, 2011, doi: 10.1038/asiamat.2011.30.

[14] J. H. Perepezko, R. I. Wu, R. Hebert, and G. Wilde, "Synthesis and Stability of Amorphous Al Alloys," *Mater. Res. Soc. Proc.*, vol. 644, p. L4.7.1-L4.7.12, 2001.

[15] A. Inoue, A. Kitamura, and T. Masumoto, "The effect of aluminium on mechanical properties and thermal stability of (Fe, Co,Ni) -Al-B ternary amorphous alloys," *J. Mater. Sci.*, vol. 16, pp. 1895–1908, 1981, doi: 10.1007/BF00745573.

[16] Y. He, G. J. Shiflet, and S. J. Poon, "Synthesis and properties of aluminum-based metallic glasses containing rare earths," *J. Alloys Compd.*, vol. 207–208, no. C, pp. 349–354, 1994, doi: 10.1016/0925-8388(94)90238-0.

[17] Y. He, S. J. Poon, and G. J. Shiflet, "Synthesis and properties of metallic glasses that contain aluminum," *Science (80-.).*, vol. 241, no. 4873, pp. 1640–1642, 1988, doi: 10.1126/science.241.4873.1640.

[18] A. Inoue, O. Katsumasa, A.-P. Tsai, and T. Masumoto, "New Amorphous Alloys with Good Ductility in Al-Y-M and Al-La-M," *Japanese Journal of Applied Physics*, vol. 27, no. 3. pp. L280–L282, 1988.

[19] J. Russo, F. Romano, and H. Tanaka, "Glass Forming Ability in Systems with Competing Orderings," *Phys. Rev. X*, vol. 8, no. 2, p. 21040, 2018, doi: 10.1103/PhysRevX.8.021040.

[20] Z. Long *et al.*, "On the new criterion to assess the glass-forming ability of metallic alloys," *Mater. Sci. Eng. A*, vol. 509, no. 1–2, pp. 23–30, 2009, doi: 10.1016/j.msea.2009.01.063.

[21] A. Inoue, "Stabilization of metallic supercooled liquid and bulk amorphous alloys," *Acta Mater.*, vol. 48, no. 1, pp. 279–306, 2000, doi: 10.1016/S1359-6454(99)00300-6.

[22] C. Suryanarayana and A. Inoue, "Metallic Glasses," *Metallic Glasses*. pp. 1–48, 2012, doi: 10.1002/9783527619528.ch3c.

[23] M. Bakkal, U. Karagüzel, and A. T. Kuzu, "Manufacturing Techniques of Bulk Metallic Glasses," *Mod. Manuf. Process.*, pp. 137–148, 2020, doi: 10.1002/9781119120384.ch6.

[24] C. Suryanarayana, "Rapid solidification processing," *Encyclopedia of Materials: Science and Technology*. 2001, doi: 10.1016/0927-796X(94)90022-1.

[25] R. C. Budhani, T. C. Goel, and K. L. Chopra, "Melt-spinning technique for preparation of metallic glasses," *Bull. Mater. Sci.*, vol. 4, no. 5, pp. 549–561, 1982, doi: 10.1007/BF02824962.

[26] Y. Shen and J. H. Perepezko, "Al-based amorphous alloys: Glass-forming ability, crystallization behavior and effects of minor alloying additions," *J. Alloys Compd.*, vol. 707, pp. 3–11, 2017, doi: 10.1016/j.jallcom.2016.11.079.

[27] R. Chatterjee, "Manufacturing of Metallic Glasses," *Adv. Mater. Manuf. Charact.*, vol. 7, no. 1, pp. 24–29, 2017.

[28] W. Gao and Z. Li, "ZnO thin films produced by magnetron sputtering," *Ceram. Int.*, vol. 30, no. 7, pp. 1155–1159, 2004, doi: 10.1016/j.ceramint.2003.12.197.

[29] B. Nair and B. G. Priyadarshini, "Process, structure, property and applications of metallic glasses," *AIMS Mater. Sci.*, vol. 3, no. 3, pp. 1022–1053, 2016, doi: 10.3934/matersci.2016.3.1022.

[30] A. Sagel, H. Sieber, H. J. Fecht, and J. H. Perepezko, "Synthesis of an amorphous Zr-Al-Ni-Cu alloy with large supercooled liquid region by cold-rolling of elemental foils," *Acta Mater.*, vol. 46, no. 12, pp. 4233–4241, 1998, doi: 10.1016/S1359-6454(98)00097-4.

[31] K. W. Jones, "Synchrotron-Radiation Induced X-Ray Emission (Srixe)," in *Handbook of X-Ray Spectrometrey*, 1999.

[32] S. Kaiser, U. Das, Y. Lu, V. Kundapur, and T. May, "Synchrotron Radiation: Applications in Diagnosis and Treatment of Malignant Brain Tumors," *Diagnostic Tech. Surg. Manag. Brain Tumors*, no. May 2014, 2011, doi: 10.5772/21639.

[33] P. Willmott, *An Introduction to Synchrotron Radiation*. 2011.

[34] C. Y. Tang and Z. Yang, *Transmission Electron Microscopy (TEM)*. Elsevier B.V., 2017.

[35] P. J. Goodhew, "General Introduction to Transmission Electron Microscopy TEM," *Aberration-Corrected Anal. Transm. Electron Microsc.*, pp. 1–19, 2011, doi: 10.1002/9781119978848.ch1.

[36] L. E. Franken, K. Grünewald, E. J. Boekema, and M. C. A. Stuart, "A Technical Introduction to Transmission Electron Microscopy for Soft-Matter: Imaging, Possibilities, Choices, and Technical Developments," *Small*, vol. 16, no. 14, 2020, doi: 10.1002/smll.201906198.

[37] T. Kelly, D. Larson, J. Bunton, and R. O. Neil, *Local Electrode Atom Probe Tomography Imago Contributors*. 2006.

[38] CAMECA, "Introduction to APT." https://www.cameca.com/products/apt/technique (accessed Sep. 02, 2021).

[39] M. K. Miller, *Atom probe tomography and the local electrode atom probe*, vol. 10, no. SUPPL. 2. 2004.

[40] Dieter G.E., *Mechanical Metallurgy*. McGraw-Hill, 1986.

[41] T. Demirtaş and Y. E. Kalay, "Kinetics of fcc-Al nanocrystallization in Al90Tb10 metallic glass," *J. Non. Cryst. Solids*, vol. 378, pp. 71–78, 2013, doi: 10.1016/j.jnoncrysol.2013.06.020.

[42] Y. E. Kalay, I. Kalay, J. Hwang, P. M. Voyles, and M. J. Kramer, "Local chemical and topological order in Al-Tb and its role in controlling nanocrystal formation," *Acta Mater.*, vol. 60, no. 3, pp. 994–1003, 2012, doi: 10.1016/j.actamat.2011.11.008.

[43] Y. E. Kalay, L. S. Chumbley, and I. E. Anderson, "Crystallization behavior in a highly driven marginal glass forming alloy," *J. Non. Cryst. Solids*, vol. 354, no. 26, pp. 3040–3048, 2008, doi: 10.1016/j.jnoncrysol.2007.12.006.

[44] C. Yildirim, M. Kutsal, R. T. Ott, M. F. Besser, M. J. Kramer, and Y. E. Kalay, "The role of amorphous precursor in phase selection hierarchy in marginal metallic glasses," *Mater. Des.*, vol. 112, pp. 479–484, 2016, doi: 10.1016/j.matdes.2016.09.060.

[45] M. Ovun, M. J. Kramer, and Y. E. Kalay, "Structural modeling of liquid and amorphous Al91Tb9by Monte Carlo simulations," *J. Non. Cryst. Solids*, vol. 405, pp. 27–32, 2014, doi: 10.1016/j.jnoncrysol.2014.08.037.

[46] M. Kutsal, "Production and characterization of aluminum-rare earth based bulk amorphous/nanocrystalline composite," Middle East Technical University, 2016.

[47] T. H. Ulucan, "Local structure and chemistry in marginal glass forming alloys," Middle East Technical University, 2020.

[48] TA Instruments, "DSC Q Series Specifications," p. 29, 2012, [Online]. Available: http://www.tainstruments.com/pdf/brochure/2012 DSC Brochure r1.pdf.

[49] ALBA, "BL04-MSPD beamline information." https://www.cells.es/en/beamlines/bl04-mspd (accessed Jul. 17, 2021).

[50] B. Hinrichsen, R. E. Dinnebier, and M. Jansen, "Powder3D: An easy to use program for data reduction and graphical presentation of large numbers of powder diffraction patterns," *Z. Krist*, vol. 23, pp. 231–236, 2004.

[51] T. Egami and S. J. L. Billinge, "Underneath the Bragg Peaks, Structural Analysis of Complex Materials," *Pergamon Mater. Ser.*, vol. 16, 2012.

[52] F. Sikan, "Production and characterization of CuZr-RE based bulk amorphous/nanocrystal composite," Middle East Technical University, 2017.

[53] K. Yang, X. H. Fan, B. Li, Y. H. Li, X. Wang, and X. X. Xu, "Non-isothermal crystallization kinetics and isothermal crystallization kinetics in supercooled liquid region of Cu-Zr-Al-Y bulk metallic glass," *Acta Metall. Sin. (English Lett.*, vol. 31, no. 3, pp. 290–298, 2017, doi: 10.1007/s40195-017-0625-0.

[54] S. Alleg, S. Souilah, and J. Joseph, "Thermal Stability of the Nanostructured Powder Mixtures Prepared by Mechanical Alloying," in *Applications of Calorimetry in a Wide Context - Differential Scanning Calorimetry, Isothermal Titration Calorimetry and Microcalorimetry*, no. iii, 2013.

[55] A. A. Soliman, "Derivation of the Kissinger equation for non-isothermal glass transition peaks," *J. Therm. Anal. Calorim.*, vol. 89, no. 2, pp. 389–392, 2007, doi: 10.1007/s10973-006-8158-1.

[56] H. E. Kissinger, "Reaction Kinetics in Differential Thermal Analysis," *Anal. Chem.*, vol. 29, no. 11, pp. 1702–1706, 1957, doi: 10.1021/ac60131a045.

[57] T. Ozawa, "A New Method of Analyzing Thermogravimetric Data," *Bull. Chem. Soc. Jpn.*, vol. 38, no. 11, pp. 1881–1886, 1965, doi: 10.1246/bcsj.38.1881.

[58] X. Zhang, "Applications of kinetic methods in thermal analysis: A review," *Eng. Sci.*, vol. 14, pp. 1–13, 2021, doi: 10.30919/es8d1132.

[59] P. Krüger, "On the relation between non-isothermal and isothermal Kolmogorov-Johnson-Mehl-Avrami crystallization kinetics," *J. Phys. Chem. Solids*, vol. 54, no. 11, pp. 1549–1555, 1993, doi: 10.1016/0022-3697(93)90349-V.

[60] D. W. Henderson, "Thermal analysis of non-isothermal crystallization kinetics in glass forming liquids," *J. Non. Cryst. Solids*, vol. 30, no. 3, pp. 301–315, 1979, doi: 10.1016/0022-3093(79)90169-8.

[61] H. B. Ke *et al.*, "Non-isothermal crystallization behavior of U-based amorphous alloy," *J. Alloys Compd.*, vol. 691, pp. 436–441, 2017, doi: 10.1016/j.jallcom.2016.08.252.

[62] L. Liu, Z. F. Wu, and L. Chen, "A kinetic study of the non-isothermal crystallization of a Zr-based bulk metallic glass," *Chinese Phys. Lett.*, vol. 19, no. 10, pp. 1483–1486, 2002, doi: 10.1088/0256-307X/19/10/326.

[63]   C. Yıldırım, "Structural and dynamical evolution of nanocrystals," Middle East Technical University, 2013.

[64]   Y. E. Kalay, C. Yeager, L. S. Chumbley, M. J. Kramer, and I. E. Anderson, "Initial crystallization in a nanostructured Al-Sm rare earth alloy," *J. Non. Cryst. Solids*, vol. 356, no. 28–30, pp. 1416–1424, 2010, doi: 10.1016/j.jnoncrysol.2010.05.005.

[65]   Y. E. Kalay, L. S. Chumbley, M. J. Kramer, and I. E. Anderson, "Local structure in marginal glass forming Al-Sm alloy," *Intermetallics*, vol. 18, no. 8, pp. 1676–1682, 2010, doi: 10.1016/j.intermet.2010.05.005.